ACS Catalysis

pubs.acs.org/acscatalysis

Research Article

Enhanced Photocatalytic CO_2 Reduction Activity over NH_2-MIL-125(Ti) by Facet Regulation

Xiao-Mei Cheng, Xiao-Yao Dao, Shi-Qing Wang, Jing Zhao,* and Wei-Yin Sun*

Cite This: *ACS Catal.* 2021, 11, 650−658

Read Online

ACCESS | Metrics & More | Article Recommendations | Supporting Information

ABSTRACT: Designation and optimization of facets of photocatalysts is an effective strategy to address the issue of facet-dependent photocatalytic reactions. However, studies regarding the facet effect of metal−organic frameworks (MOFs) on the photocatalytic process are in infancy. In this study, NH_2-MIL-125(Ti) with different ratios of {001} and {111} facets was exactly controlled and synthesized, and it was found that the activity in photoreduction of CO_2 is enhanced with gradually increasing exposed proportion of {111} facets. The {111} facets exhibit photocatalytic activity with the maximal CO and CH_4 yields of 8.25 and 1.01 μmol g^{-1} h^{-1}, which are 9 and 5 times higher than those of {001} facets, respectively. Also, the {111} facets give the highest quantum yields of 0.14 and 0.07% for CO and CH_4 production, respectively. Steady-state and time-resolved fluorescence spectra reveal the importance of inhibiting the recombination of photoinduced electrons and holes for the sample with {111} facets. Besides, Ti^{III} formed during the reaction process exhibits strong reducibility for CO_2. Starting from NH_2-MIL-125(Ti), the photocatalytic performance can be enhanced by regulating exposed {111} facets. This work not only provides a strategy for further enhancing photocatalytic performance by tuning the exposed active facets of MOFs, but also provides a deep understanding of the factors for improving the photocatalytic reduction of CO_2.

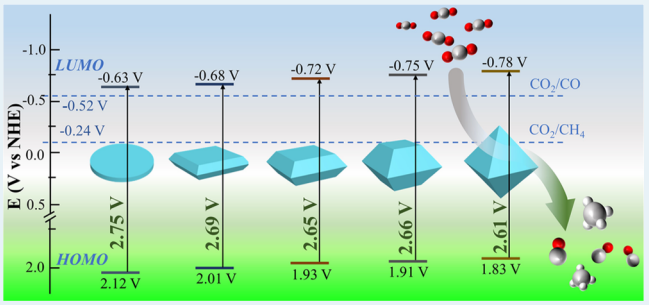

KEYWORDS: *NH_2-MIL-125(Ti), facets, metal−organic frameworks, CO_2 reduction, photocatalytic reaction*

1. INTRODUCTION

Photoreduction of CO_2 to generate valuable fuels and chemical feedstocks is considered as an effective way to alleviate the greenhouse effect and address the energy issues.[1−3] However, the inertness of the CO_2 molecule and inherent defects of the photocatalyst lead to low efficiency of photocatalytic CO_2 reduction.[4−6] To overcome these drawbacks, enormous efforts have been made for metal−organic frameworks (MOFs) to improve the activity of photoreduction of CO_2, including heterojunction construction, cocatalyst loading, and surface engineering.[7−11] Owing to the catalytic reactions that mainly occur on the surface of the catalysts, the optical and chemical properties of catalysts are largely dependent on the degree of exposed facets.[12−14] Also, the optimization of surface structure is favor of electron generation and spatial separation, which are crucial for photoreduction of CO_2.[15−17] Thus, we focus our attention on exploring the regulation of the surface facet of MOFs and its influence on the activity of CO_2 photoreduction.[18]

MOFs, as a type of inorganic−organic hybrid materials with a high surface area, tunable porosity, and tailorable structure, show definite advantages concerning the capability of precisely designed and optimized surface structure.[19−24] There are reports about morphology and facet control of MOFs in the past decades, which provided supports for our work.[25−27] Particularly, the titanium-based MOF, NH_2-MIL-125(Ti) with high chemical stability and significant optical response, is one of the most efficient photocatalysts for H_2 generation, organic pollutant degradation, and CO_2 photoreduction.[28−31] To improve the photocatalytic efficiency of NH_2-MIL-125(Ti), the common way is to load cocatalysts, such as noble metals, inorganic semiconductors, and functional materials.[32,33] For example, amorphous TiO_2-decorated NH_2-MIL-125(Ti) composites enhanced the activity of photocatalytic CO_2 to CH_4 conversion, which was 1.7 times higher than that of pure NH_2-MIL-125(Ti).[34] Composite photocatalyst g-C_3N_4/CuO@NH_2-MIL-125(Ti) achieved by encapsulating CuO quantum dots and combining with g-C_3N_4 exhibits remarkably improved activity of CO_2 photoreduction and charge separation efficiency.[35]

Received: October 12, 2020
Revised: December 17, 2020
Published: December 30, 2020

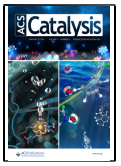

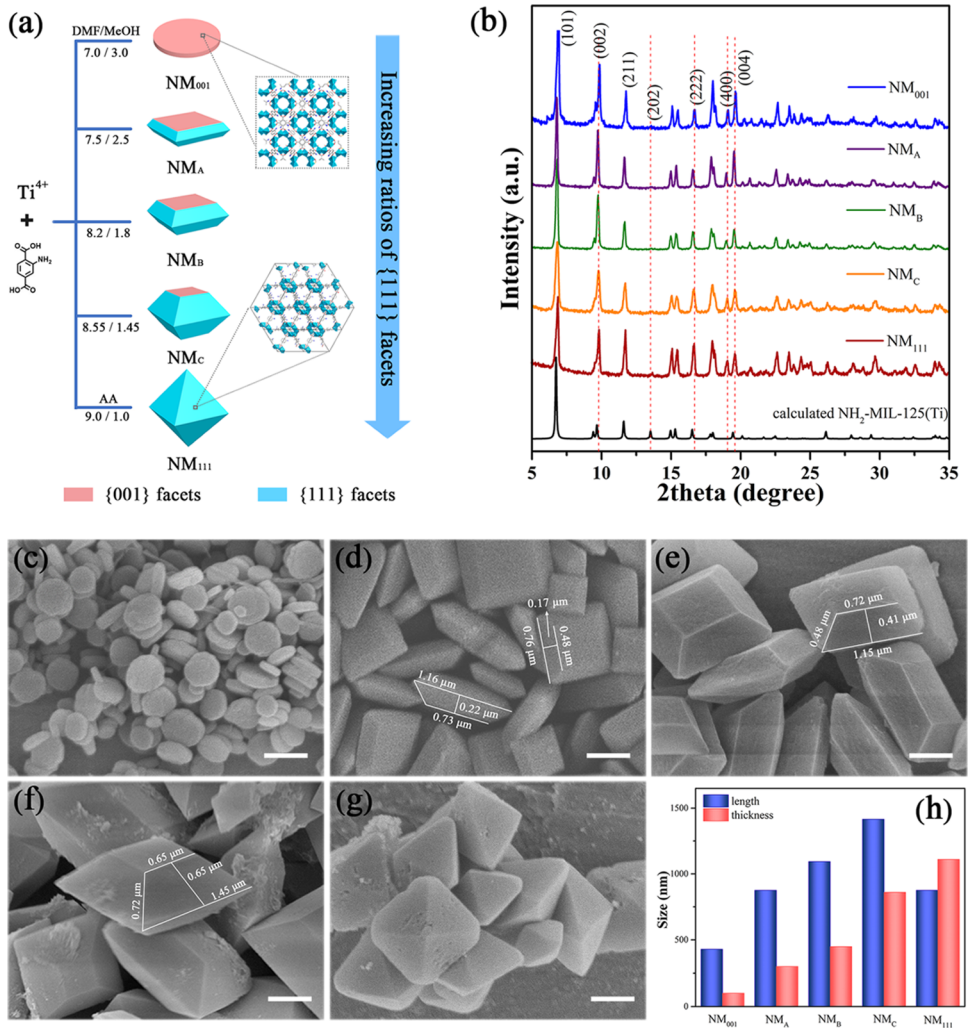

Figure 1. (a) Schematic illustration of the evolution of morphology and facet over NH_2-MIL-125(Ti). (b) PXRD patterns of as-synthesized photocatalysts and calculated NH_2-MIL-125(Ti). SEM spectra of NM_{001} (c), NM_A (d), NM_B (e), NM_C (f), and NM_{111} (g) and average sizes (h) of as-synthesized NH_2-MIL-125(Ti). Scale bar: 500 nm.

Herein, we report NH_2-MIL-125(Ti) for photoreduction of CO_2 focused on the impact of facet regulation for photocatalytic activity. The {001}, {111}, and co-exposed {001} and {111} facets of NH_2-MIL-125(Ti) were successfully fabricated with morphologies of disk, octahedron, and truncated octahedrons, respectively. They exhibit excellent photoreduction activity for CO_2 to CO and CO_2 to CH_4 conversion. Importantly, the {111} facets possess a large specific surface area and superior CO_2 uptake, which provide more active sites for the reduction reaction. Likewise, the content of Ti atoms in {111} facets is higher than that in {001} facets, Ti^{III} in favor of accelerating the progress of reduction reaction by unveiling more active sites during the reaction process. The {111} facets exhibit optimal photocatalytic activity for CO_2 reduction ascribed to the fast electron transfer and effectively suppressed recombination of electron−hole pairs. Besides, regulating the active facets is beneficial to broaden the absorption range, reconstruct the electronic structure, and prolong the lifetimes of photogenerated electrons of NH_2-MIL-125(Ti).

2. EXPERIMENTAL SECTION

2.1. Preparation of NH_2-MIL-125(Ti) with Different Exposed Facets. In a typical experiment, NH_2-BDC and modulator (acetic acid, AA) were dissolved in MeOH and DMF mixture solution to a total volume of 10 mL. Then, a titanium source was added and mixed with sonication for 5 min. The specific amounts of reactants and modulators in the synthesis are presented in Table S1 (see the Supporting Information). The obtained solution was transferred into the Teflon-line steel autoclave and kept in an oven at 150 °C for 24 h. The yellow powders were isolated by centrifugation, thoroughly washed with DMF and MeOH several times, and dried under vacuum for 5 h at 80 °C.

3. RESULTS AND DISCUSSION

In the synthetic system, we identified that the volume ratio of DMF and MeOH is powerful to adjust the ratio of {001} and {111} facets. These samples are denoted as NM_{001}, NM_A, NM_B, NM_C, and NM_{111}, where NM represents NH_2-MIL-125(Ti); 001 and 111 are the dominant facets; and A, B, and C are the mixed {001} and {111} facets with different ratios. Tuning the solvent ratio of DMF and MeOH and different titanium sources of titanium tetraisopropanolate (TPOT) or titanium butoxide (TBOT) with or without a modulator of AA can achieve transition of the morphology and facet for NH_2-MIL-125(Ti) (Figure 1a). For further observation of the

https://dx.doi.org/10.1021/acscatal.0c04426
ACS Catal. 2021, 11, 650−658

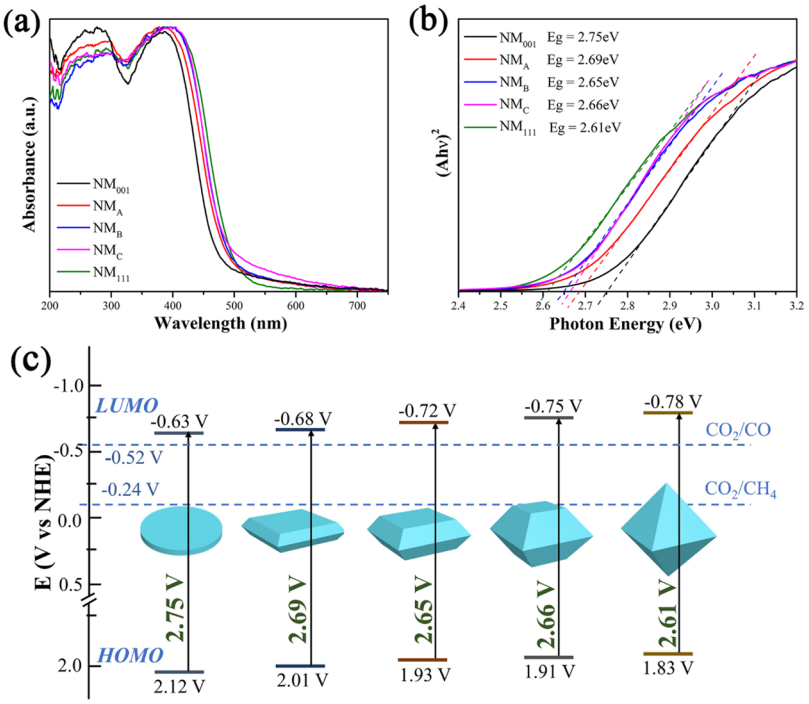

Figure 2. (a) UV−vis diffuse reflectance spectra, (b) Tauc plots, and (c) HOMO−LUMO gap of the as-synthesized photocatalysts.

evolution of the morphology and facet of all samples directly, scanning electron microscopy (SEM) images were obtained. Clearly, these well-faceted NH_2-MIL-125(Ti) can be easily identified as {001} and {111} facets according to the SEM. The disk-shaped NH_2-MIL-125(Ti) exposes two {001} facets on the top and bottom (Figure 1c). Along with the variation of tuning factors (Table S1), the {001} facets are gradually diminished, and the {111} facets appeared and increased (Figure 1d−f). Until the last sample shown in Figure 1g, {001} facets disappeared, and the {111} facets were exposed completely. The results demonstrate the evolution of as-synthesized NH_2-MIL-125(Ti) facets from {001} to {111}. The average sizes of the samples are displayed in Figure 1h. The average percentages of exposed {001} and {111} facets were calculated from the corresponding facet area as illustrated in Scheme S1 (Table S3).[36]

Powder X-ray diffraction (PXRD) patterns of the as-synthesized samples are shown in Figure 1b, which confirm that all the samples matched well with the calculated NH_2-MIL-125(Ti).[37] It is noteworthy that the relative intensity of (101) and (202) crystallographic planes at 6.7 and 13.5° reduced and disappeared, respectively. Furthermore, compared with the calculated NH_2-MIL-125(Ti), the relative intensity of (222) facet at 16.6° increased gradually from NM_{001} to NM_{111}. The (*hkl*) denotes Miller indices of the facet, and {*hkl*} indicates a family index of the crystal facet.[38] XRD peaks reflect the distribution of atom arrays in the facet of samples, and facet-dependent PXRD patterns indicate that the surfaces of NM_{001} and NM_{111} are dominated by {001} and {111} facets, respectively, as discussed previously.[28] The facet-dependent PXRD patterns are consistent with the morphology and facet observed by SEM. The Fourier transform infrared (FT-IR) spectra are shown in Figure S1 to further clarify the functional groups of NH_2-MIL-125(Ti). Thermogravimetric analyses reveal that NH_2-MIL-125(Ti) with different exposed facets have similar thermal stability (Figure S2). These characterizations indicate that NH_2-MIL-125(Ti) with varied proportions of exposed {001} and {111} facets were successfully achieved.

To investigate the optical properties of these samples, UV−vis diffuse reflectance spectra were examined. The results indicate that all samples display light absorption from the UV to visible region (Figure 2a). The prepared samples mainly exhibit two absorption bands around 300 and 400 nm, corresponding to the absorption of Ti−O_x clusters and ligand-based absorption within the framework of MOFs.[35,39] The absorption wavelength shows red shift with increasing the ratios of {111} facets of the samples. The NM_{111} displays the maximal red-shifted absorption wavelength, while NM_{001} gives the narrowest absorption. Tauc plots were used to estimate the highest occupied molecular orbital (HOMO)−lowest unoccupied molecular orbital (LUMO) gap, as depicted in Figure 2b. For semiconductor-like MOFs, the HOMO−LUMO gap is defined as the gap between the HOMO and the LUMO according to the molecular orbital model. To estimate the HOMO−LUMO gap edges of the catalysts, the Mott−Schottky plots were measured (Figures S3−S7). The flat band potentials were determined to be −0.63, −0.68, −0.72, −0.75, and −0.78 V versus NHE for NM_{001}, NM_A, NM_B, NM_C, and NM_{111}, respectively. Thus, the calculated HOMO−LUMO gaps are 2.75 eV (NM_{001}), 2.69 eV (NM_A), 2.65 eV (NM_B), 2.66 eV (NM_C), and 2.61 eV (NM_{111}), as shown in Figure 2c. The catalyst with a lower HOMO−LUMO gap requires light with lower energy to inspire photogenerated electrons and holes. Accordingly, the exposure of {111} facets in NH_2-MIL-125(Ti) is favorable for possessing a better photoresponse under simulated sunlight irradiation and decreasing the energy of photoexcited electrons.

According to the optical behavior of these samples, we explored their photocatalytic performance for CO_2 reduction and evaluated the correlation between photocatalytic activity and facets of the as-synthesized NH_2-MIL-125(Ti). The

https://dx.doi.org/10.1021/acscatal.0c04426
ACS Catal. 2021, 11, 650−658

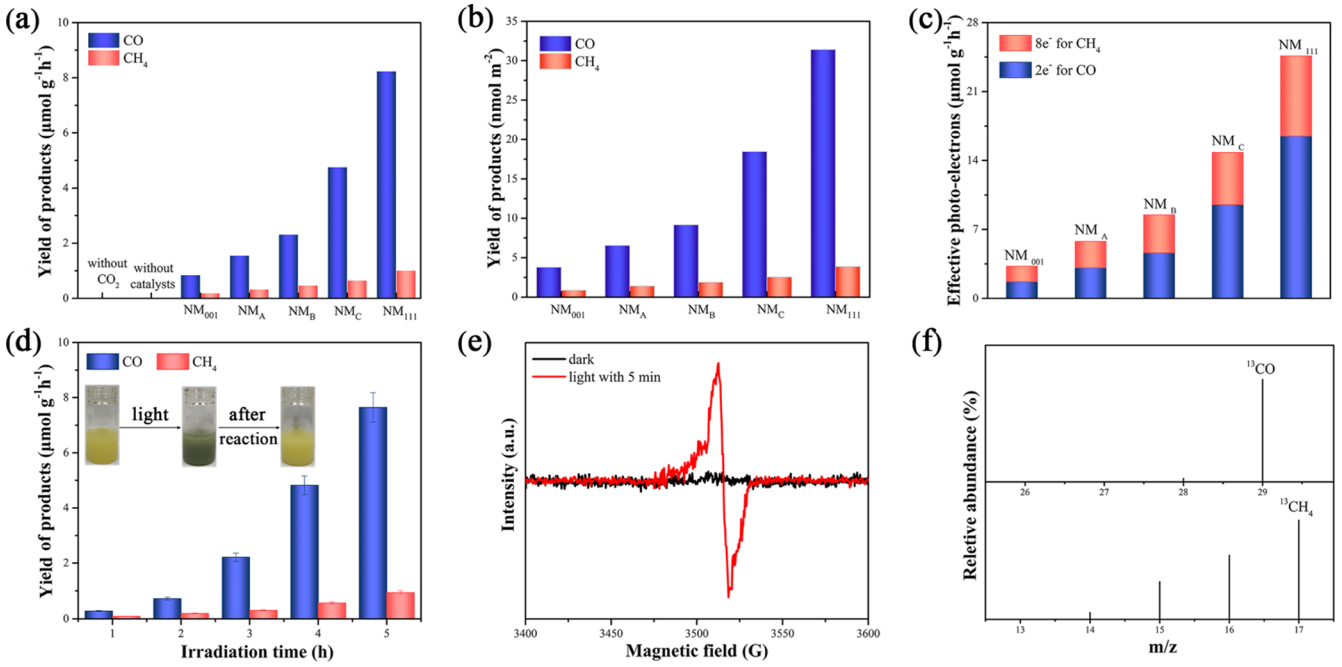

Figure 3. Yields of products with respect to the mass of catalysts (a) and with respect to the facet surface area (b), effective photoelectrons of CO and CH_4 under visible light irradiation (5 h) of the as-synthesized photocatalysts (c), irradiation time-dependence evolution of CO and CH_4 of NM_{111} (d), EPR spectra of NM_{111} in the dark and upon irradiation for 5 min (e), mass spectral analysis for photoreduction of $^{13}CO_2$ to ^{13}CO (m/z = 29) and $^{13}CH_4$ (m/z = 17) using NM_{111} as the photocatalyst (f).

photocatalytic CO_2-to-CO and CO_2-to-CH_4 conversions of the samples are depicted in Figure 3a. The CO and CH_4 characterized peaks are monitored by an FID detector (Figure S8). The NM_{111} exhibits superior photocatalytic activity for generation of CO and CH_4 with product yields of 8.25 and 1.01 μmol g^{-1} h^{-1}, which are 9 and 5 times higher than those of NM_{001}, respectively. Also, NM_{111} gives the highest quantum yields (QYs) of 0.14 and 0.07% for CO and CH_4 production (Table S4), which are comparable or higher than some reported photocatalysts (Tables S5 and S6). Interestingly, the trend of the product yields with respect to the facet surface area is consistent with the mass of catalysts (Figure 3a,b), and NM_{111} shows the best performance (Figure 3b).[40,41] Upon irradiation, the reduction reaction proceeded, in which TEOA acts as a proton and electron donor, providing $2e^-$ and $8e^-$ for reduction products of CO and CH_4, respectively (Figure 3c). The degradation product of TEOA is determined as 2-(bis(2-hydroxyethyl)amino)acetaldehyde (Figures S9 and S10). The ^{1}H NMR spectrum is used to prove that no liquid product was generated during the photocatalytic reaction (Figure S11). To verify that the detected CO and CH_4 are generated via the photocatalytic CO_2 reduction, we performed comparison experiments. No C_1 products can be detected with absent CO_2 or photocatalyst. To further confirm the carbon source of the CO and CH_4 products, the ^{13}C-isotope trace experiment was employed using $^{13}CO_2$ as the substrate. The products were analyzed by gas chromatography−mass spectrometry (GC−MS). The signal peaks at m/z = 29 (^{13}CO) and m/z = 17 ($^{13}CH_4$) are observed (Figure 3f). The irradiation time-dependence evolution of CO and CH_4 during 5 h is given in Figure 3d, and the intriguing phenomenon of the photochromic effect was observed in this photocatalytic system (inset in Figure 3d). The color changed from original bright yellow to green with constant irradiation and then turned to the yellow after the photocatalytic reaction. This process is attributed to the interconversion between Ti^{IV} and Ti^{III} valent states in the Ti−O_x cluster with transition of the photogenerated electrons.[42] Furthermore, electron paramagnetic resonance (EPR) spectra were measured to elucidate the existence of Ti^{III}. As revealed in Figure 3e, no EPR signal was detected in the dark, while an obvious peak was observed with a g factor of 1.948 upon irradiation for 5 min.[43,44] The results provide clues to further ensure the existence of Ti^{III}, indicating the conversion of Ti^{IV} to Ti^{III} in the photoreduction system. It is noteworthy that NM_{111} exhibits excellent stability after five cycles, and the photoreduction activity was maintained above 85% compared with the initial test (Figure S12). The PXRD pattern (Figure S13), FT-IR spectra (Figure S14), and SEM image (Figure S15) of NM_{111} after five recycles confirm the structure stability under the photocatalytic reaction conditions.

To further explore the facet effect on the photocatalytic CO_2 reduction, N_2 adsorption isotherms were measured to obtain specific surface areas of the as-synthesized samples. As shown in Figure S16, all samples exhibit type I isotherms at 77 K with strong N_2 uptakes at a low relative pressure (P/P_0 < 0.001).[45,46] NM_{111} possesses the largest specific surface area (1312.2 cm^3 g^{-1}) among all the samples. The specific surface areas are found to increase with the increasing percentages of exposed {111} facets. Moreover, the adsorption abilities of these photocatalysts were investigated with catalytic substrate CO_2, and CO_2 adsorption isotherms are obtained at 273 (Figure S17) and 298 K (Figure S18), showing the relatively large amounts CO_2 uptakes of NM_{111}. The specific surface areas and the CO_2 uptakes are listed in Table S3. The high specific surface area and superior CO_2 uptake ability of NM_{111} provide more active sites for enhanced photocatalytic CO_2 reduction activity.[47]

The survey spectra of X-ray photoelectron spectroscopy (XPS) are provided in Figure S19, and high-resolution XPS (HR−XPS) was employed to estimate the chemical state and

https://dx.doi.org/10.1021/acscatal.0c04426
ACS Catal. 2021, 11, 650−658

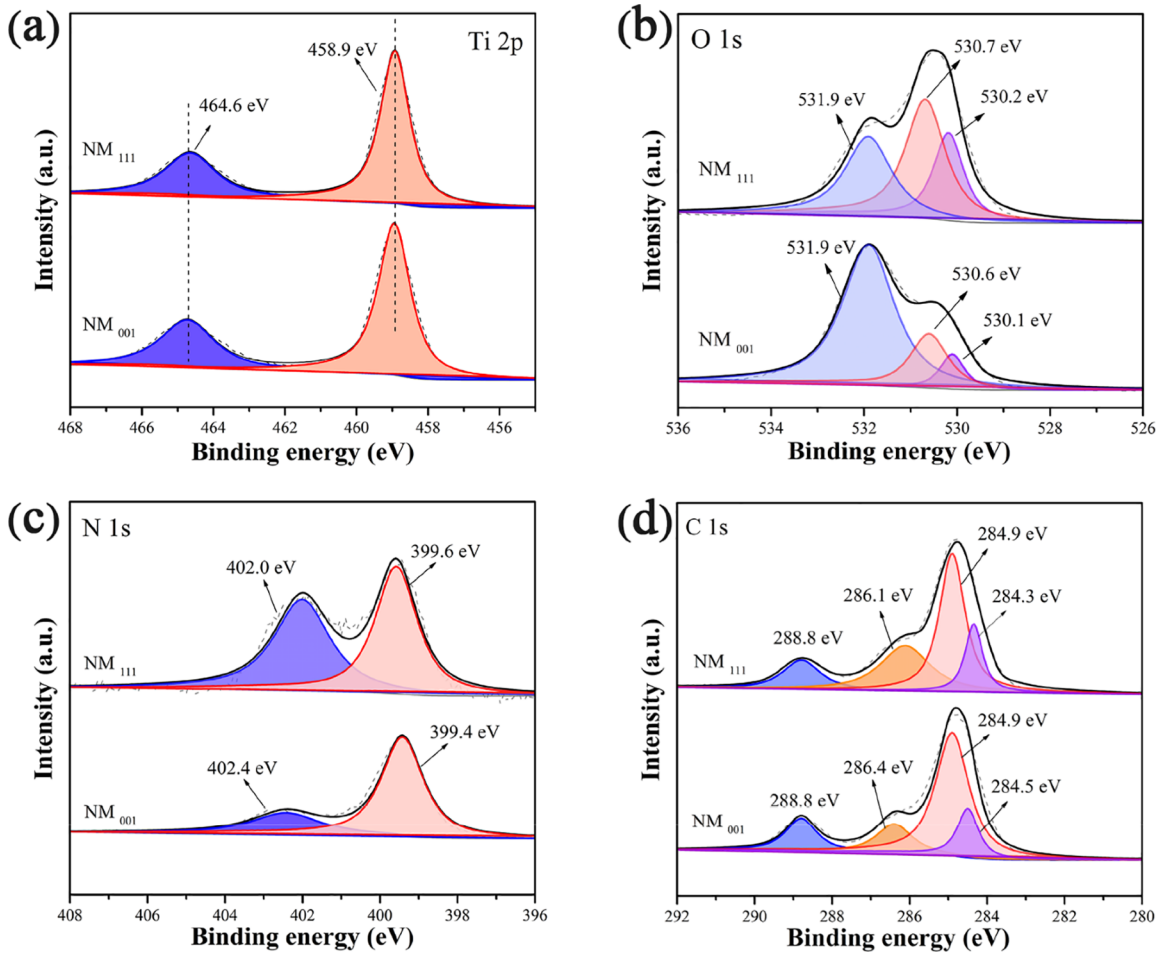

Figure 4. HR−XPS spectra of Ti 2p (a), O 1s (b), N 1s (c), and C 1s (d) of NM_{111} and NM_{001}.

coordination environment of NM_{111} and NM_{001}. As shown in Figure 4a, the Ti 2p displays two binding energy peaks at 458.9 and 464.6 eV, which is attributed to Ti $2p_{3/2}$ and Ti $2p_{1/2}$ of Ti^{IV}, respectively, indicating that titanium bonded to oxygen in the Ti−O_x cluster remained in Ti^{IV}.[48] High-resolution O 1s presents distinction between NM_{111} and NM_{001} with three fitted peaks (Figure 4b). The first peak located at 531.9 eV is assigned to the oxygen in the carboxylate group in NH_2-BDC, while the other two peaks at 530.7 and 530.2 eV are ascribed to oxygen in the Ti−O_x cluster of NM_{111}.[49] The observed peak intensities are clearly higher than those of NM_{001}, indicating that more Ti−O_x clusters are exposed in the {111} facets in NM_{111}. The atomic concentrations of NM_{111} and NM_{001} are listed in Table S2. NM_{111} exhibits higher Ti atomic concentration than NM_{001}, demonstrating more exposure of Ti−O_x clusters on the surface of NM_{111}. The structure of {001} and {111} facets in NH_2-MIL-125(Ti) revealed the distinct distribution of Ti−O_x on different facets (Figures S20 and S21). As shown in Figure 4c, high-resolution N 1s presents two peaks corresponding to the −NH−$^+$ and $-NH_2$ in amino groups of NM_{111} and NM_{001}, respectively.[50] Obviously, the binding energy at 402.0 eV of NM_{111} is stronger than that of NM_{001}, implying the stronger electron transfer in NM_{111}. The results demonstrate abundant Ti−O_x clusters and the vigorous electron transfer on the surface of NM_{111}, which further improve the photocatalytic activity.

In addition to UV−vis spectra, steady photoluminescence (PL) spectral measurements were carried out to in-depth investigate photoinduced charge separation properties (Figure 5a). Under the excitation wavelength of 325 nm, NM_{001} shows a high-intensity fluorescence at 485 nm due to the fast recombination of charge carriers, while PL intensity decreased significantly with the increase of the percentages of the {111} facets. Such appearance indicates the low recombination rate of photoinduced charge carriers and the effective separation of photogeneration electrons and holes in {111} facets. The time-resolved fluorescence decay spectra were performed to explore the photogeneration carrier dynamics of these as-synthesized photocatalysts (Figure 5b). The charge-separated lifetime increases in the order of NM_{001} (0.17 ns) < NM_A (0.94 ns) < NM_B (1.19 ns) < NM_C (1.25 ns) < NM_{111} (1.63 ns), generally corresponding to a trend of prolonged lifetimes with the increase in the exposure of {111} facets. In the present case, the longer fluorescence lifetimes are attributed to the fast transfer of photoinduced charge carriers and inhibition of the recombination of photogenerated electrons and holes.[51] The effective electronic interactions among these photocatalysts were investigated by the photocurrent transient response measurement (Figure 5c). All the catalysts exhibited a clear photocurrent response under on−off simulated sunlight irradiation. NM_{001} shows lower photocurrent density due to the fast recombination of photogeneration charge carriers. The photocurrent signal increases with the increase of the ratio of exposed {111} facets, and NM_{111} possesses the largest photocurrent response, revealing that the NM_{111} has capability of interface charge transfer and separation. Besides, the results

https://dx.doi.org/10.1021/acscatal.0c04426
ACS Catal. 2021, 11, 650−658

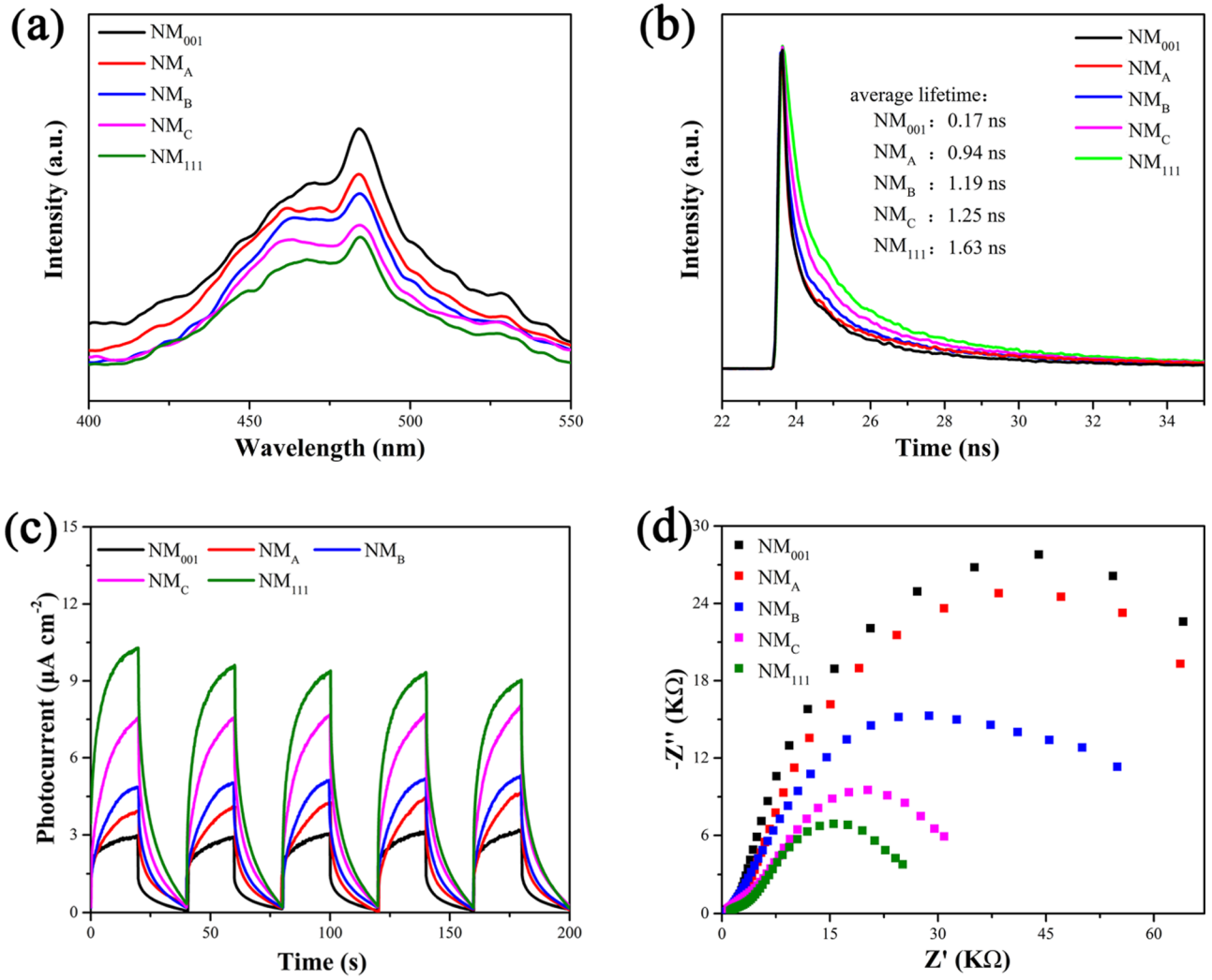

Figure 5. (a) Steady photoluminescence spectra under 325 nm excitation, (b) time-resolved fluorescence decay spectra, (c) photocurrent transient response, and (d) EIS Nyquist plots of the as-synthesized photocatalysts.

are also supported by electrochemical impedance spectroscopy (EIS) (Figure 5d). The charge transfer resistance (R_{ct}) of NM_{111} is much lower than that of NM_{001}, NM_A, NM_B, and NM_C, indicating the favorable electron transfer of NM_{111} during the light irradiation.

Based on the above results, we proposed a possible mechanism for enhancing the photocatalytic activity of CO_2 reduction of NH_2-MIL-125(Ti) with exposed varied ratios of {001} and {111} facets (Scheme 1). First, the high LUMO value of NM_{111} reaches −0.78 V (vs NHE) with a strong ability to realize CO_2-to-CO (−0.52 V) and CO_2-to-CH_4 (−0.24 V) conversions.[17,52] Photogenerated electrons are excited from the HOMO under simulated light irradiation owing to the lower HOMO−LUMO gap and then migrate to LUMO to trigger the reduction reaction, while the photogenerated holes participate in the oxidation reaction. Second, TEOA as a sacrificial agent in this photocatalytic system will be oxidized, providing electrons to the photocatalytic system in the meantime. Third, high specific surface area and superior CO_2 uptake ability provide efficient active sites. Ti^{IV} in the NH_2-MIL-125(Ti) captures the electron and converts to Ti^{III}, and the Ti^{III} sites possess strong reducibility to realize the conversion of CO_2 to the CO and CH_4 products. The NM_{111} photocatalyst effectively suppresses the recombination

Scheme 1. Proposed Mechanism of NM_{111} for Photoreduction CO_2 to CO and CH_4

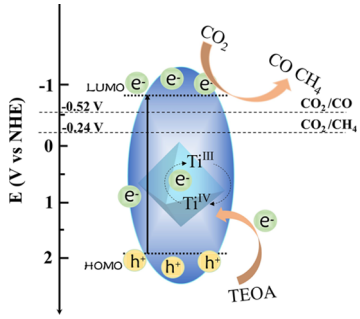

of photogenerated electrons and holes. Thus, a lot of electrons and holes participate in the photocatalytic reaction and further promote the photocatalytic activity of CO_2 reduction.

4. CONCLUSIONS

In summary, we accurately designed and successfully synthesized a series of NH_2-MIL-125(Ti) with varied ratios of {111} facets by one-step solvothermal method, achieving the exact control of active exposed facets and comprehensively

https://dx.doi.org/10.1021/acscatal.0c04426
ACS Catal. 2021, 11, 650−658

evaluating the ability of photocatalytic CO_2 reduction of the as-synthesized photocatalysts. We also realized the optimization of CO_2 photoreduction activity with 100% exposure of {111} facets. The enhanced photoreduction of CO_2 activity was attributed to the exposure of {111} facets, which not only enlarge the specific surface area and CO_2 adsorption, prolong the PL lifetime, and increase the Ti atomic concentrations but also rapidly spatial separate and effectively suppress the recombination of electrons and holes. The transition between Ti^{IV} and Ti^{III} has been considered in the photoreaction, which facilitated the photoreduction process and enhanced photocatalytic activity. The NM_{111} sample could be readily achieved by solvothermal reaction, and further efforts are needed to enhance the activity by incorporating composite species and/or optimize the CO_2 reduction product such as CH_4. This work demonstrates the intriguing investigation of the facet effect of NH_2-MIL-125(Ti), which paves new ways for designing efficient MOF catalysts for photocatalytic performance by regulating the exposed active facets. The challenges in exploring the facet effect in MOFs still remain, and more efforts may be required in the future.

■ ASSOCIATED CONTENT

Supporting Information

The Supporting Information is available free of charge at https://pubs.acs.org/doi/10.1021/acscatal.0c04426.

FT-IR, TG, Mott−Schottky plots, ESI−MS, NMR, SEM images, PXRD, N_2 and CO_2 adsorption, XPS, structures, synthetic system, atomic concentration facet ratio, QY, and comparison of photocatalytic CO_2 reduction (PDF)

■ AUTHOR INFORMATION

Corresponding Authors

Jing Zhao − *State Key Laboratory of Coordination Chemistry, Chemistry and Biomedicine Innovation Center (ChemBIC), School of Chemistry and Chemical Engineering, Nanjing University, Nanjing 210023, China;* orcid.org/0000-0001-5177-5699; Email: jingzhao@nju.edu.cn

Wei-Yin Sun − *Coordination Chemistry Institute, State Key Laboratory of Coordination Chemistry, School of Chemistry and Chemical Engineering, Nanjing National Laboratory of Microstructures, Collaborative Innovation Center of Advanced Microstructures, Nanjing University, Nanjing 210023, China;* orcid.org/0000-0001-8966-9728; Email: sunwy@nju.edu.cn

Authors

Xiao-Mei Cheng − *Coordination Chemistry Institute, State Key Laboratory of Coordination Chemistry, School of Chemistry and Chemical Engineering, Nanjing National Laboratory of Microstructures, Collaborative Innovation Center of Advanced Microstructures, Nanjing University, Nanjing 210023, China; State Key Laboratory of Coordination Chemistry, Chemistry and Biomedicine Innovation Center (ChemBIC), School of Chemistry and Chemical Engineering, Nanjing University, Nanjing 210023, China*

Xiao-Yao Dao − *Coordination Chemistry Institute, State Key Laboratory of Coordination Chemistry, School of Chemistry and Chemical Engineering, Nanjing National Laboratory of Microstructures, Collaborative Innovation Center of Advanced Microstructures, Nanjing University, Nanjing 210023, China*

Shi-Qing Wang − *Coordination Chemistry Institute, State Key Laboratory of Coordination Chemistry, School of Chemistry and Chemical Engineering, Nanjing National Laboratory of Microstructures, Collaborative Innovation Center of Advanced Microstructures, Nanjing University, Nanjing 210023, China*

Complete contact information is available at: https://pubs.acs.org/10.1021/acscatal.0c04426

Notes

The authors declare no competing financial interest.

■ ACKNOWLEDGMENTS

We gratefully acknowledge the National Basic Research Program of China (grant no. 2017YFA0303504) and the Fundamental Research Funds for the Central Universities (grant no. 14380232) for financial support of this work. This work was also supported by a Project Funded by the Priority Academic Program Development of Jiangsu Higher Education Institutions.

■ REFERENCES

(1) Wu, Y. A.; McNulty, I.; Liu, C.; Lau, K. C.; Liu, Q.; Paulikas, A. P.; Sun, C.-J.; Cai, Z.; Guest, J. R.; Ren, Y.; Stamenkovic, V.; Curtiss, L. A.; Liu, Y.; Rajh, T. Facet-Dependent Active Sites of a Single Cu_2O Particle Photocatalyst for CO_2 Reduction to Methanol. *Nat. Energy* **2019**, *4*, 957−968.

(2) Lin, L.; Lin, Z.; Zhang, J.; Cai, X.; Lin, W.; Yu, Z.; Wang, X. Molecular-Level Insights on the Reactive Facet of Carbon Nitride Single Crystals Photocatalysing overall Water Splitting. *Nat. Catal.* **2020**, *3*, 649−655.

(3) Wang, S.; Liu, G.; Wang, L. Crystal Facet Engineering of Photoelectrodes for Photoelectrochemical Water Splitting. *Chem. Rev.* **2019**, *119*, 5192−5247.

(4) Wang, Y.; Liu, X.; Zheng, C.; Li, Y.; Jia, S.; Li, Z.; Zhao, Y. Tailoring TiO_2 Nanotube-Interlaced Graphite Carbon Nitride Nanosheets for Improving Visible-Light-Driven Photocatalytic Performance. *Adv. Sci.* **2018**, *5*, 1700844−1700852.

(5) Remiro-Buenamañana, S.; Cabrero-Antonino, M.; Martínez-Guante, M.; Álvaro, M.; Navalón, S.; García, H. Influence of Co-catalysts on the Photocatalytic Activity of MIL-125(Ti)-NH_2 in the overall Water Splitting. *Appl. Catal., B* **2019**, *254*, 677−684.

(6) Zhang, H. X.; Hong, Q. L.; Li, J.; Wang, F.; Huang, X.; Chen, S.; Tu, W.; Yu, D.; Xu, R.; Zhou, T.; Zhang, J. Isolated Square-Planar Copper Center in Boron Imidazolate Nanocages for Photocatalytic Reduction of CO_2 to CO. *Angew. Chem., Int. Ed.* **2019**, *58*, 11752−11756.

(7) Zhao, L.; Zhao, Z.; Li, Y.; Chu, X.; Li, Z.; Qu, Y.; Bai, L.; Jing, L. The Synthesis of Interface-Modulated Ultrathin Ni(II) MOF/g-C_3N_4 Heterojunctions as Efficient Photocatalysts for CO_2 Reduction. *Nanoscale* **2020**, *12*, 10010−10018.

(8) Feng, X.; Pi, Y.; Song, Y.; Brzezinski, C.; Xu, Z.; Li, Z.; Lin, W. Metal-Organic Frameworks Significantly Enhance Photocatalytic Hydrogen Evolution and CO_2 Reduction with Earth-Abundant Copper Photosensitizers. *J. Am. Chem. Soc.* **2020**, *142*, 690−695.

(9) Deng, X.; Yang, L.; Huang, H.; Yang, Y.; Feng, S.; Zeng, M.; Li, Q.; Xu, D. Shape-Defined Hollow Structural Co-MOF-74 and Metal Nanoparticles@Co-MOF-74 Composite Through a Transformation Strategy for Enhanced Photocatalysis Performance. *Small* **2019**, *15*, 1902287−1902294.

(10) Chen, L.; Wang, Y.; Yu, F.; Shen, X.; Duan, C. A Simple Strategy for Engineering Heterostructures of Au Nanoparticle-Loaded Metal-Organic Framework Nanosheets to Achieve Plasmon-Enhanced

Photocatalytic CO_2 Conversion under Visible Light. *J. Mater. Chem. A* **2019**, *7*, 11355−11361.
(11) Ran, J.; Jaroniec, M.; Qiao, S.-Z. Cocatalysts in Semiconductor-Based Photocatalytic CO_2 Reduction: Achievements, Challenges, and Opportunities. *Adv. Mater.* **2018**, *30*, 1704649.
(12) Mu, L.; Zhao, Y.; Li, A.; Wang, S.; Wang, Z.; Yang, J.; Wang, Y.; Liu, T.; Chen, R.; Zhu, J.; Fan, F.; Li, R.; Li, C. Enhancing Charge Separation on High Symmetry $SrTiO_3$ Exposed with Anisotropic Facets for Photocatalytic Water Splitting. *Energy Environ. Sci.* **2016**, *9*, 2463−2469.
(13) Pan, J.; Liu, G.; Lu, G. Q. M.; Cheng, H.-M. On the True Photoreactivity Order of {001}, {010}, and {101} Facets of Anatase TiO_2 Crystals. *Angew. Chem., Int. Ed.* **2011**, *50*, 2133−2137.
(14) Sun, S.; Gao, P.; Yang, Y.; Yang, P.; Chen, Y.; Wang, Y. N-Doped TiO_2 Nanobelts with Coexposed (001) and (101) Facets and Their Highly Efficient Visible-Light-Driven Photocatalytic Hydrogen Production. *ACS Appl. Mater. Interfaces* **2016**, *8*, 18126−18131.
(15) Li, R.; Zhang, W.; Zhou, K. Metal-Organic-Framework-Based Catalysts for Photoreduction of CO_2. *Adv. Mater.* **2018**, *30*, 1705512−1705542.
(16) Dao, X.-Y.; Guo, J.-H.; Wei, Y.-P.; Guo, F.; Liu, Y.; Sun, W.-Y. Solvent-Free Photoreduction of CO_2 to CO Catalyzed by Fe-MOFs with Superior Selectivity. *Inorg. Chem.* **2019**, *58*, 8517−8524.
(17) Li, K.; Peng, B.; Peng, T. Recent Advances in Heterogeneous Photocatalytic CO_2 Conversion to Solar Fuels. *ACS Catal.* **2016**, *6*, 7485−7527.
(18) Yang, W.; Wang, H. J.; Liu, R. R.; Zhang, C.; Li, C.; Zhong, D. C.; Lu, T. B. Tailoring crystal facets of metal-organic layers to enhance photocatalytic activity for CO_2 reduction. *Angew. Chem., Int. Ed.* **2021**, *60*, 409−414.
(19) Jiao, L.; Wang, Y.; Jiang, H.-L.; Xu, Q. Metal-Organic Frameworks as Platforms for Catalytic Applications. *Adv. Mater.* **2018**, *30*, 1703663−1703685.
(20) Kang, Y.-S.; Lu, Y.; Chen, K.; Zhao, Y.; Wang, P.; Sun, W.-Y. Metal-Organic Frameworks with Catalytic Centers: From Synthesis to Catalytic Application. *Coord. Chem. Rev.* **2019**, *378*, 262−280.
(21) Li, F. L.; Wang, P.; Huang, X.; Young, D. J.; Wang, H. F.; Braunstein, P.; Lang, J. P. Large-Scale, Bottom-Up Synthesis of Binary Metal-Organic Framework Nanosheets for Efficient Water Oxidation. *Angew. Chem., Int. Ed.* **2019**, *58*, 7051−7056.
(22) Liu, D.; Lang, J.-P.; Abrahams, B. F. Highly Efficient Separation of a Solid Mixture of Naphthalene and Anthracene by a Reusable Porous Metal-Organic Framework Through a Single-Crystal-to-Single-Crystal Transformation. *J. Am. Chem. Soc.* **2011**, *133*, 11042−11045.
(23) Li, F.-L.; Shao, Q.; Huang, X.; Lang, J.-P. Nanoscale Trimetallic Metal-Organic Framework Enable Efficient Oxygen Evolution Electrocatalysis. *Angew. Chem., Int. Ed.* **2018**, *57*, 1888−1892.
(24) Liu, C.-Y.; Chen, X.-R.; Chen, H.-X.; Niu, Z.; Hirao, H.; Braunstein, P.; Lang, J.-P. Ultrafast Luminescent Light-Up Guest Detection Based on the Lock of the Host Molecular Vibration. *J. Am. Chem. Soc.* **2020**, *142*, 6690−6697.
(25) Liu, X.-Y.; Lo, W.-S.; Wu, C.; Williams, B. P.; Luo, L.; Li, Y.; Chou, L.-Y.; Lee, Y.; Tsung, C.-K. Tuning Metal-Organic Framework Nanocrystal Shape Through Facet-Dependent Coordination. *Nano Lett.* **2020**, *20*, 1774−1780.
(26) Liu, Q.; Jin, L.-N.; Sun, W.-Y. Facile Fabrication and Adsorption Property of a Nano/Microporous Coordination Polymer with Controllable Size and Morphology. *Chem. Commun.* **2012**, *48*, 8814−8816.
(27) Liu, Q.; Yang, J.-M.; Jin, L.-N.; Sun, W.-Y. Controlled Synthesis of Porous Coordination-Polymer Microcrystals with Definite Morphologies and Sizes under Mild Conditions. *Chem. —Eur. J.* **2014**, *20*, 14783−14789.
(28) Guo, F.; Guo, J.-H.; Wang, P.; Kang, Y.-S.; Liu, Y.; Zhao, J.; Sun, W.-Y. Facet-Dependent Photocatalytic Hydrogen Production of Metal-Organic Framework NH_2-MIL-125(Ti). *Chem. Sci.* **2019**, *10*, 4834−4838.
(29) Liu, H.; Zhang, J.; Ao, D. Construction of Heterostructured $ZnIn_2S_4$@NH_2-MIL-125(Ti) Nanocomposites for Visible-Light-Driven H_2 Production. *Appl. Catal., B* **2018**, *221*, 433−442.
(30) Li, S.; Ji, K.; Zhang, M.; He, C.; Wang, J.; Li, Z. Boosting the Photocatalytic CO_2 Reduction of Metal-Organic Frameworks by Encapsulating Carbon Dots. *Nanoscale* **2020**, *12*, 9533−9540.
(31) Li, L.; Wang, X. S.; Liu, T. F.; Ye, J. Titanium-Based MOF Materials: From Crystal Engineering to Photocatalysis. *Small Methods* **2020**, *4*, 2000486−2000514.
(32) Khaletskaya, K.; Pougin, A.; Medishetty, R.; Rösler, C.; Wiktor, C.; Strunk, J.; Fischer, R. A. Fabrication of Gold/Titania Photocatalyst for CO_2 Reduction Based on Pyrolytic Conversion of the Metal-Organic Framework NH_2-MIL-125(Ti) Loaded with Gold Nanoparticles. *Chem. Mater.* **2015**, *27*, 7248−7257.
(33) Yan, B.; Zhang, L.; Tang, Z.; Al-Mamun, M.; Zhao, H.; Su, X. Palladium-Decorated Hierarchical Titania Constructed from the Metal-Organic Frameworks NH_2-MIL-125(Ti) as a Robust Photocatalyst for Hydrogen Evolution. *Appl. Catal., B* **2017**, *218*, 743−750.
(34) Hu, J.; Ding, J.; Zhong, Q. In Situ Fabrication of Amorphous TiO_2/NH_2-MIL-125(Ti) for Enhanced Photocatalytic CO_2 into CH_4 with H_2O under Visible-Light Irradiation. *J. Colloid Interface Sci.* **2020**, *560*, 857−865.
(35) Li, N.; Liu, X.; Zhou, J.; Chen, W.; Liu, M. Encapsulating CuO Quantum Dots in MIL-125(Ti) Coupled with g-C_3N_4 for Efficient Photocatalytic CO_2 Reduction. *Chem. Eng. J.* **2020**, *399*, 125782−125792.
(36) Liu, S.; Yu, J.; Jaroniec, M. Anatase TiO_2 with Dominant High-Energy {001} Facets: Synthesis, Properties, and Applications. *Chem. Mater.* **2011**, *23*, 4085−4093.
(37) Smalley, A. P.; Reid, D. G.; Tan, J. C.; Lloyd, G. O. Alternative Synthetic Methodology for Amide Formation in the Post-Synthetic Modification of Ti-MIL125-NH_2. *CrystEngComm* **2013**, *15*, 9368−9371.
(38) Quan, Z.; Wang, Y.; Fang, J. High-Index Faceted Noble Metal Nanocrystals. *Acc. Chem. Res.* **2013**, *46*, 191−202.
(39) Kim, S.-N.; Kim, J.; Kim, H.-Y.; Cho, H.-Y.; Ahn, W.-S. Adsorption/Catalytic Properties of MIL-125 and NH_2-MIL-125. *Catal. Today* **2013**, *204*, 85−93.
(40) Melchionna, M.; Fornasiero, P. Updates on the Roadmap for Photocatalysis. *ACS Catal.* **2020**, *10*, 5493−5501.
(41) Beltram, A.; Romero-Ocaña, I.; Josè Delgado Jaen, J.; Montini, T.; Fornasiero, P. Photocatalytic Valorization of Ethanol and Glycerol over TiO_2 Polymorphs for Sustainable Hydrogen Production. *Appl. Catal., A* **2016**, *518*, 167−175.
(42) Huang, H.; Wang, X.-S.; Philo, D.; Ichihara, F.; Song, H.; Li, Y.; Li, D.; Qiu, T.; Wang, S.; Ye, J. Toward Visible-Light-Assisted Photocatalytic Nitrogen Fixation: A Titanium Metal Organic Framework with Functionalized Ligands. *Appl. Catal., B* **2020**, *267*, 118686−118692.
(43) Nasalevich, M. A.; Becker, R.; Ramos-Fernandez, E. V.; Castellanos, S.; Veber, S. L.; Fedin, M. V.; Kapteijn, F.; Reek, J. N. H.; van der Vlugt, J. I.; Gascon, J. Co@NH_2-MIL-125(Ti): Cobaloxime-Derived Metal-Organic Framework-Based Composite for Light-Driven H_2 Production. *Energy Environ. Sci.* **2015**, *8*, 364−375.
(44) Xiao, H.; Zhang, W.; Yao, Q.; Huang, L.; Chen, L.; Boury, B.; Chen, Z. Zn-free MOFs like MIL-53(Al) and MIL-125(Ti) for the Preparation of Defect-Rich, Ultrafine ZnO Nanosheets with High Photocatalytic Performance. *Appl. Catal., B* **2019**, *244*, 719−731.
(45) Chambers, M. B.; Wang, X.; Ellezam, L.; Ersen, O.; Fontecave, M.; Sanchez, C.; Rozes, L.; Mellot-Draznieks, C. Maximizing the Photocatalytic Activity of Metal-Organic Frameworks with Aminated-Functionalized Linkers: Substoichiometric Effects in MIL-125-NH_2. *J. Am. Chem. Soc.* **2017**, *139*, 8222−8228.
(46) Wang, S.; Xu, M.; Peng, T.; Zhang, C.; Li, T.; Hussain, I.; Wang, J. Y.; Tan, B. Porous Hypercrosslinked Polymer-TiO_2-Graphene Composite Photocatalysts for Visible-Light-Driven CO_2 Conversion. *Nat. Commun.* **2019**, *10*, 676−685.
(47) Wang, X.-K.; Liu, J.; Zhang, L.; Dong, L.-Z.; Li, S.-L.; Kan, Y.-H.; Li, D.-S.; Lan, Y.-Q. Monometallic Catalytic Models Hosted in

Stable Metal-Organic Frameworks for Tunable CO_2 Photoreduction. *ACS Catal.* **2019**, *9*, 1726−1732.
(48) Zhang, B.; Zhang, J.; Tan, X.; Shao, D.; Shi, J.; Zheng, L.; Zhang, J.; Yang, G.; Han, B. MIL-125-NH_2@TiO_2 Core-Shell Particles Produced by a Post-Solvothermal Route for High-Performance Photocatalytic H_2 Production. *ACS Appl. Mater. Interfaces* **2018**, *10*, 16418−16423.
(49) Lan, K.; Liu, Y.; Zhang, W.; Liu, Y.; Elzatahry, A.; Wang, R.; Xia, Y.; Al-Dhayan, D.; Zheng, N.; Zhao, D. Uniform Ordered Two-Dimensional Mesoporous TiO_2 Nanosheets from Hydrothermal-Induced Solvent-Confined Monomicelle Assembly. *J. Am. Chem. Soc.* **2018**, *140*, 4135−4143.
(50) Wang, H.; Yuan, X.; Wu, Y.; Zeng, X.; Leng, L.; Wu, Z.; Jiang, L.; Li, H. Facile Synthesis of Amino-Functionalized Titanium Metal-Organic Frameworks and Their Superior Visible-Light Photocatalytic Activity for Cr(VI) Reduction. *J. Hazard. Mater.* **2015**, *286*, 187−194.
(51) Zhou, M.; Wang, S.; Yang, P.; Huang, C.; Wang, X. Boron Carbon Nitride Semiconductors Decorated with CdS Nanoparticles for Photocatalytic Reduction of CO_2. *ACS Catal.* **2018**, *8*, 4928−4936.
(52) Xiang, Q.; Cheng, B.; Yu, J. Graphene-Based Photocatalysts for Solar-Fuel Generation. *Angew. Chem., Int. Ed.* **2015**, *54*, 11350−11366.

https://dx.doi.org/10.1021/acscatal.0c04426
ACS Catal. 2021, 11, 650−658

Supporting Information

Enhanced Photocatalytic CO_2 Reduction Activity over NH_2-MIL-125(Ti) by Facet Regulation

Xiao-Mei Cheng,[†,‡] Xiao-Yao Dao,[†] Shi-Qing Wang,[†] Jing Zhao,*[,‡] and Wei-Yin Sun*[,†]

[†]Coordination Chemistry Institute, State Key Laboratory of Coordination Chemistry, School of Chemistry and Chemical Engineering, Nanjing National Laboratory of Microstructures, Collaborative Innovation Center of Advanced Microstructures, Nanjing University, Nanjing 210023, China

[‡]State Key Laboratory of Coordination Chemistry, Chemistry and Biomedicine Innovation Center (ChemBIC), School of Chemistry and Chemical Engineering, Nanjing University, Nanjing, 210023, China

Corresponding Author e-mail:

*jingzhao@nju.edu.cn

*sunwy@nju.edu.cn

EXPERIMENTAL SECTION

Chemicals. Titanium tetraisopropanolate (TPOT), titanium butoxide (TBOT), 2-aminoterephthalic acid (NH_2-BDC) and triethanolamine (TEOA) were purchased from Aladdin Industrial Corporation. Solvents such as N,N-dimethylformamide (DMF) and methanol (MeOH) are of reagent grade obtained from Sinopharm Chemical Reagent Co., Ltd. All chemicals are of analytical grade and used directly without further purification.

Characterization. Powder X-ray diffraction (PXRD) patterns were obtained on a Bruker D8 Advance X-ray diffractometer with Cu Kα radiation (1.5478 Å). Scanning electron microscope (SEM) were carried out on a Hitachi S-4800 at an acceleration voltage of 5 kV.

Fourier transform infrared (FT-IR) spectra were recorded using KBr disc in the range of 400-4000 cm^{-1} on a Bruker Vector 22. X-ray photoelectron spectroscopy (XPS) were obtaned on UIVAC-PHI 5000 Versa Probe with monochromated Al Kα radiation (hν = 1486.6 eV) spectrophotometer, binding energies were calibrated by using the C 1s peak (284.8 eV). UV-Vis diffuse reflectance spectra (DRS) were measured on a Shimadzu UV-3600 spectrophotometer. Thermogravimetric analyses (TGA) were performed on a TGA-DSC1 thermal analyzer (Mettler-Toledo Instrumentation). The electron paramagnetic resonance (EPR) was measured at room temperature on an A220-9.5/12 (Bruker). All the gas adsorption isotherms were measured on a Belsorp-max volumetric gas sorption analyzer. Before sorption measurements, all samples were degassed at 120 °C for 6 h. Photoluminescence spectra (PL) were measured on an Aminco Bowman Series2 spectrofluorometer. Time-resolved fluorescence decay spectra were obtained at room temperature on a HORIBA Jobin Yvon FL-3 spectrometer. The $^{13}CO_2$ isotopic labelling experiments were performed using a gas chromatography-mass spectrometer with a TG-5MS column (Trace GC Ultra, ThermoFisher Scientific).

Photoelectrochemical Measurements. Transient photocurrent measurements were performed on a CHI 730E electrochemical workstation in a standard three-electrode system with the photocatalyst-coated ITO as working electrode, graphite rod and Ag/AgCl electrode as counter and reference electrode,respectively. Na_2SO_4 solution was used as the electrolyte. The 2 mg of sample was added into Nafion (10 μL) and methanol (1.0 mL) mixed solution, and dropped the suspension (300 μL) onto the ITO plate with about 1 cm^2 area.

Photocatalytic CO_2 Reduction Experiments. The photocatalytic reactions were performed in CEL-SPH2N-D9, CeAulight, China equipped with a homemade photoreactor (d = 5 cm) together with a condensate circulating water filter to shield the photothermal effect. Firstly, photocatalysts (10 mg) were scattered in MeCN (15 mL) and water (1 mL) with TEOA

(3 ml) as a sacrificial agent. In the evacuation reaction system, pure CO_2 gas was injected into the closed system with condenser circulation pump (test temperature: 4 ℃). A 300 W xenon arc lamp with AM 1.5G filter was used as the light source. The gas products were monitored by gas chromatography (GC-9860) equipped with FID detector. All photocatalytic data were repeated at least three times. Recycling experiments were performed under similar conditions by using collected catalyst instead of the fresh one.

Quantum Yield Calculation. The quantum yield of CO_2 photocatalytic conversion in 5 h can be calculated by Eqs. (1) and (2). Two and eight electrons are required to convert CO_2 to CO and CH_4, respectively.[1, 2]

$$\phi_{CO}\ (\%)=\frac{2\times\text{mole of CO formation}}{\text{mole of photons absorbed by photocatalyst}} \quad (1)$$

$$\phi_{CH_4}\ (\%)=\frac{8\times\text{mole of } CH_4 \text{ formation}}{\text{mole of photons absorbed by photocatalyst}} \quad (2)$$

The number of moles of photons absorbed by photocatalyst (MPAP) during 5 h was calculated by Eq. (3).

$$\text{MPAP}=\frac{\text{absobed photon flux } \left(\frac{\mu W}{cm^2}\right)\times\text{outer surface area of reactor } \left(cm^2\right)\times\text{radiation time (s)}}{\text{each photo energy J}\times(6.02\times10^{23})} \quad (3)$$

Calculations of the percentages of {001} and {111} facets. Based on the SEM results, we can obtain the geometrical parameters of NH_2-MIL-125(Ti) with different exposed facets through statistic according to SEM images. Then we can calculate the percentages of different facets in the as-synthesized NH_2-MIL-125(Ti). A case study of truncated octahedron is shown Scheme S1.

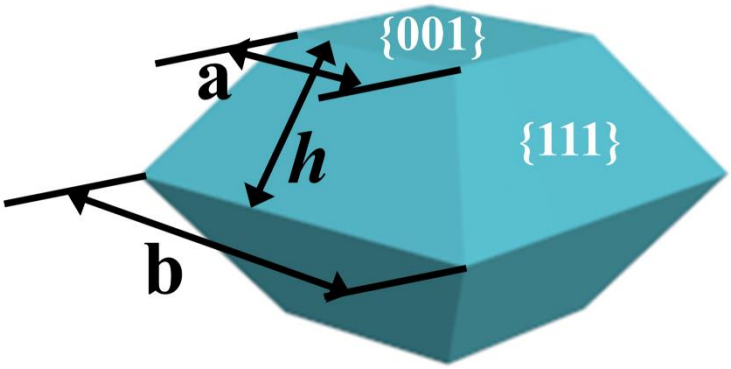

Scheme S1. Geometric model of NH2-MIL-125(Ti) with {001} and {111} facets exposed.

$$S_{001}=a^2$$

$$S_{111}=\frac{1}{2}(a+b)\times h$$

$$P_{001}=\frac{S_{001}\times 2}{S_{111}\times 8+S_{001}\times 2}$$

$$P_{111}=\frac{S_{111}\times 2}{S_{111}\times 8+S_{001}\times 2}$$

According to the above equations, the percentages of {001} and {111} facets in the as-synthesized NH_2-MIL-125(Ti) are calculated.

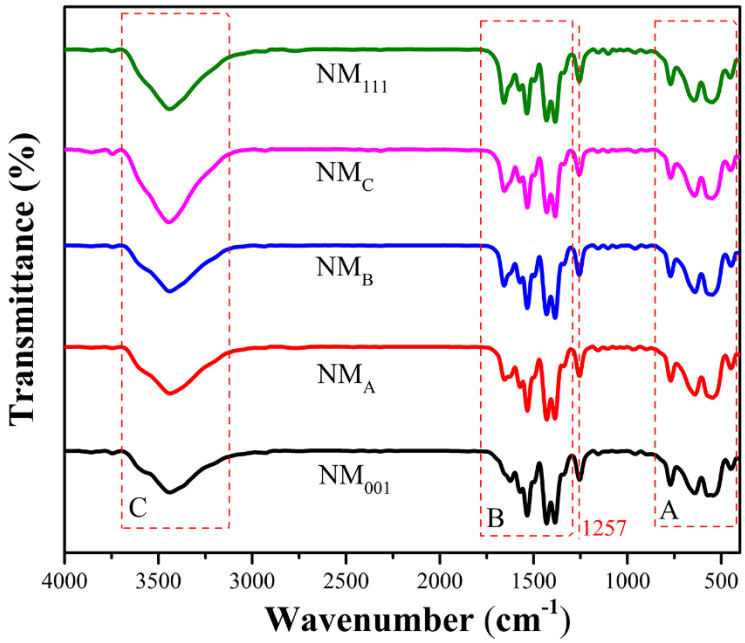

Figure S1. FT-IR spectra of as-synthesized NH_2-MIL-125(Ti).

In the FT-IR spectra, the large broad band in the range of 3200 ~ 3700 cm^{-1} is originated from the amino group and free solvent molecules in the pores. In the region of 1400 ~ 1709 cm^{-1} there are typical vibrational bands attributed to the carboxylate groups of the linkers in the framework of NH_2-MIL-125(Ti). The characteristic O-Ti-O vibrations are located in the range of 400 ~ 800 cm^{-1}. Besides, the strong band at 1257 cm^{-1} belongs to the C-N stretching vibration from the aromatic amine. [3-5]

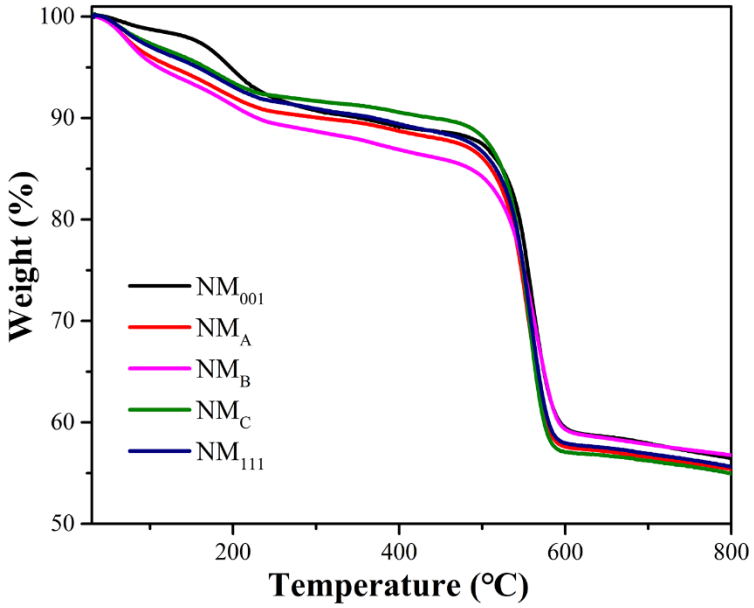

Figure S2. TG curves of as-synthesized NH_2-MIL-125(Ti).

All TG curves show two-step weight loss. The first step is to release the solvent molecules within the pores from 60 to 200 ℃, and the second one from 300 ℃ is due to the collapse of the framework of NH_2-MIL-125(Ti).

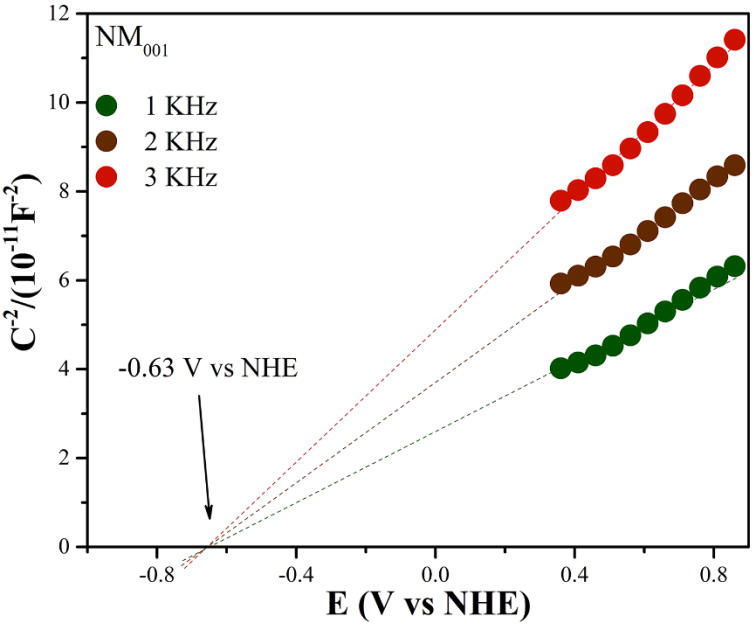

Figure S3. Mott-Schottky plot of as-synthesized NM_{001}.

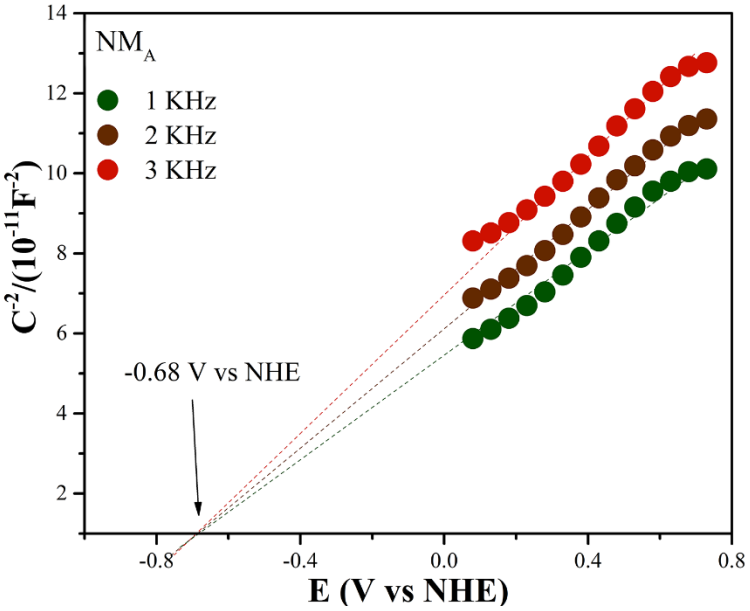

Figure S4. Mott-Schottky plot of as-synthesized NM_A.

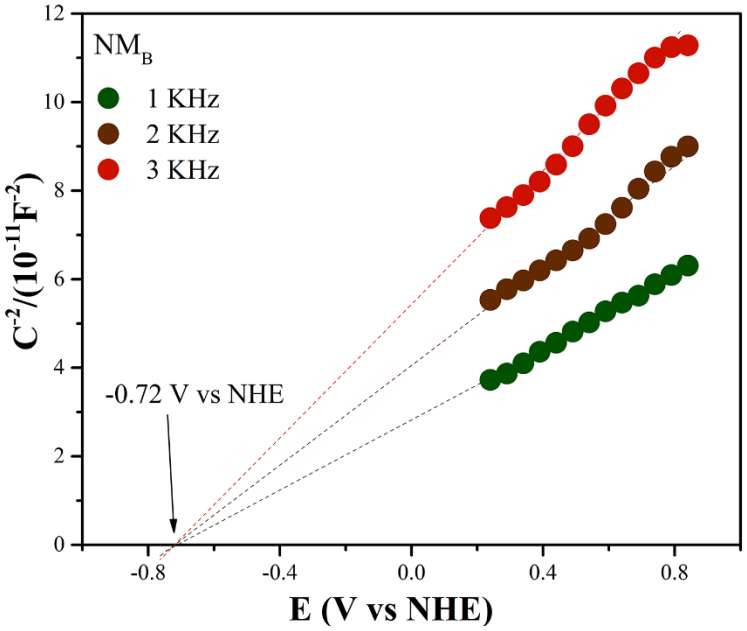

Figure S5. Mott-Schottky plot of as-synthesized NM_B.

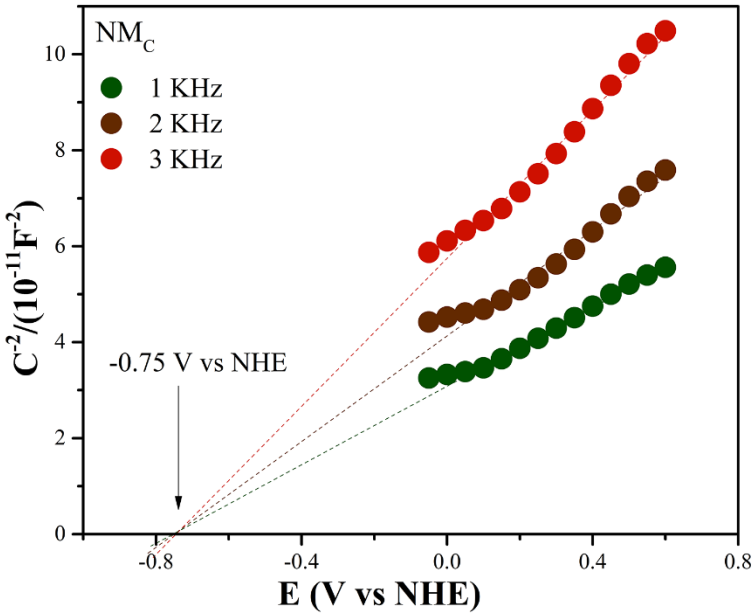

Figure S6. Mott-Schottky plot of as-synthesized NM_C.

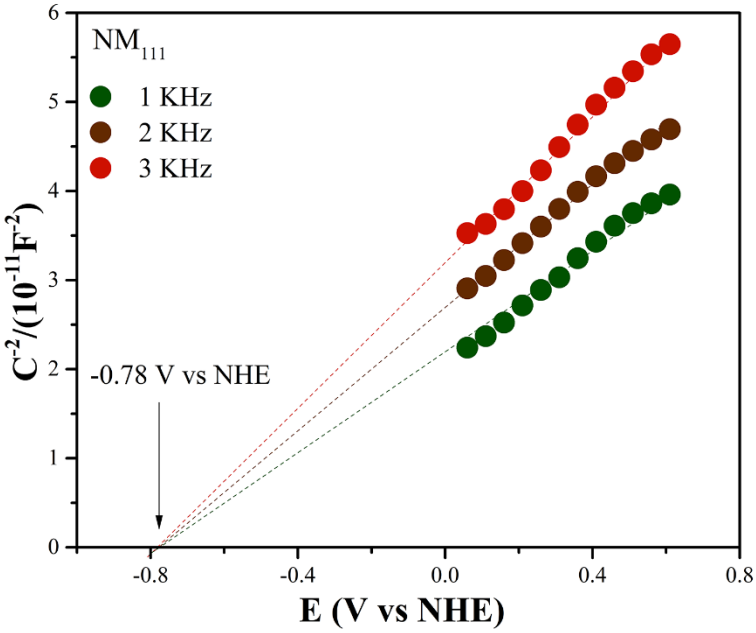

Figure S7. Mott-Schottky plot of as-synthesized NM_{111}.

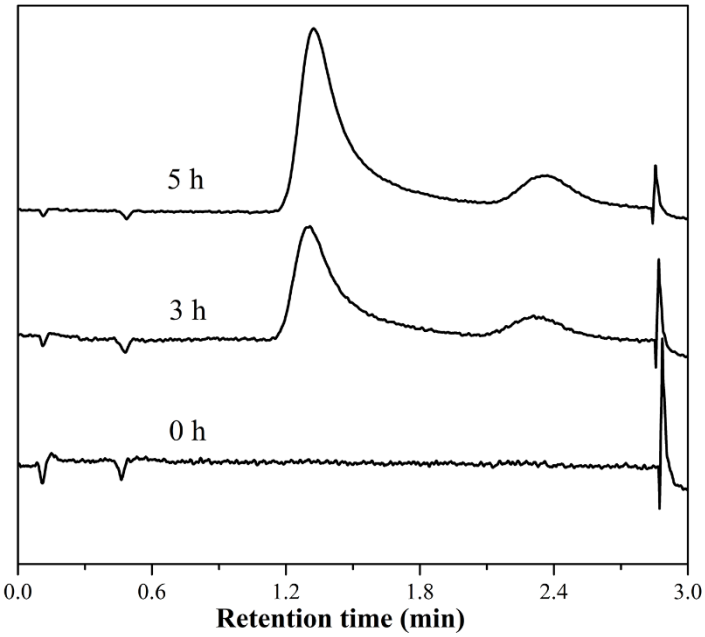

Figure S8. FID detector for CO and CH_4 monitoring from irradiation analyzed by gas chromatograms of NM_{111}. Retention time of CO is 1.290 min, and CH_4 was detected in 2.370 min.

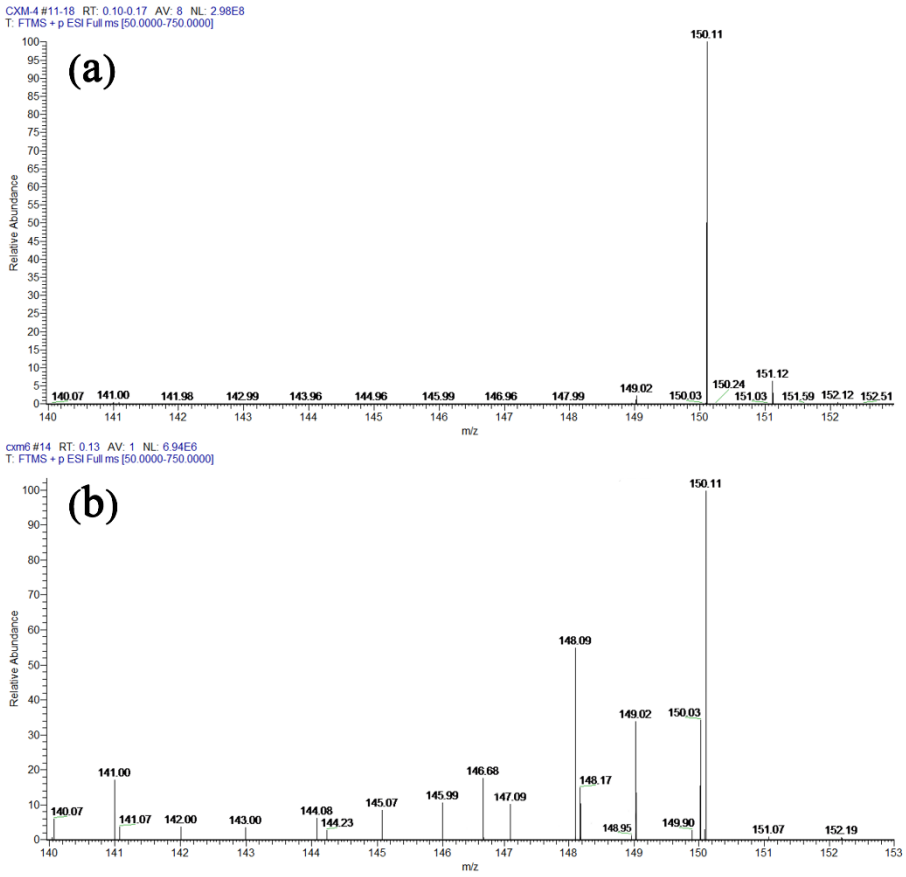

Figure S9. ESI-MS spectra for TEOA before and after reaction.

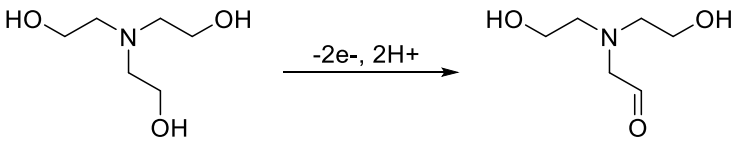

Figure S10. Possible degradation product of TEOA during the process of photocatalytic reaction.

In the photocatalytic reduction reaction, TEOA as a sacrificing agent was degraded.[6, 7] ESI-MS spectroscopy was used to detect the possible degradation products of TEOA. Figure S9 shows the changes of TEOA before and after the reaction. After reaction for 5 h, a peak at m/z = 148 was observed, which is assigned to the oxidation product of TEOA, namely 2-(bis(2-hydroxyethyl)amino)acetaldehyde (Figure S10).[8, 9]

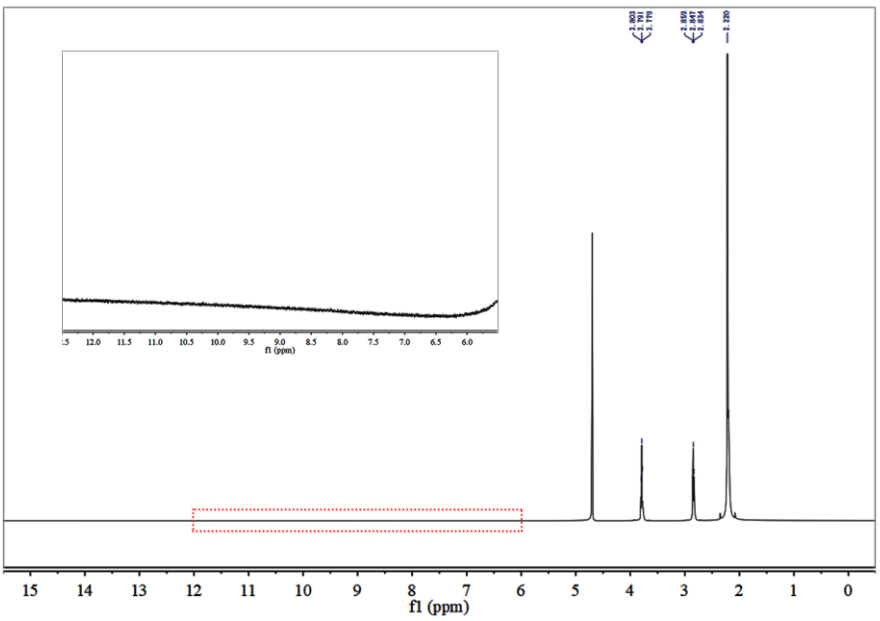

Figure S11. ^{1}H-NMR spectrum was used to detect the liquid product from the photocatalytic reaction of as-synthesized NM_{111}.

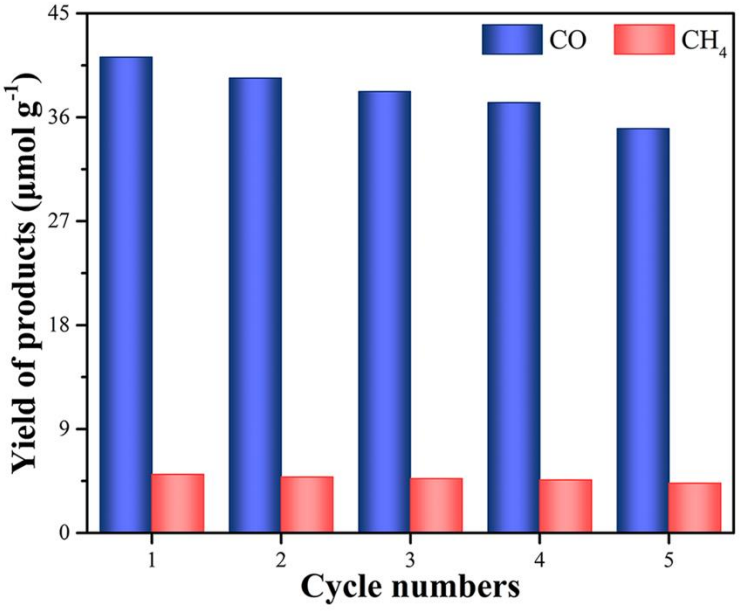

Figure S12. Recycle tests over the NM_{111}.

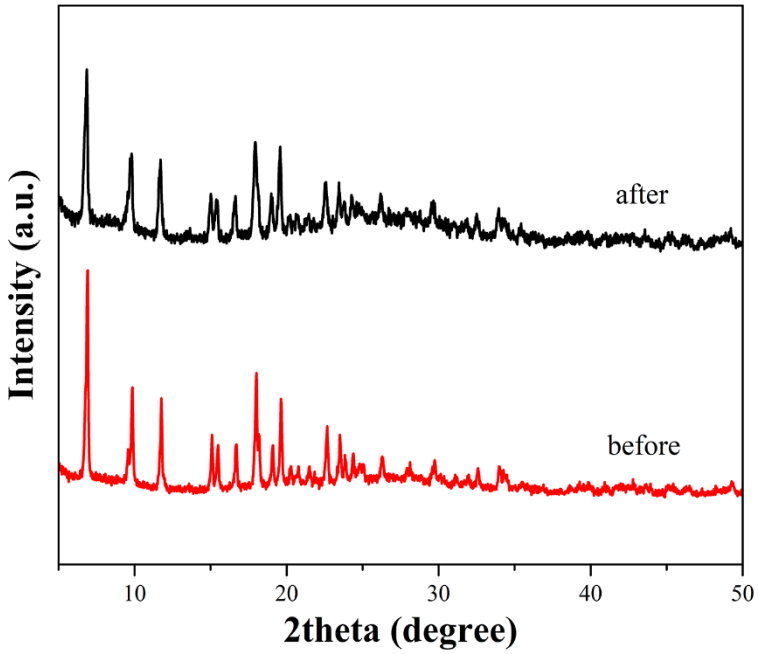

Figure S13. PXRD of NM_{111} before and after photocatalytic CO_2 reduction.

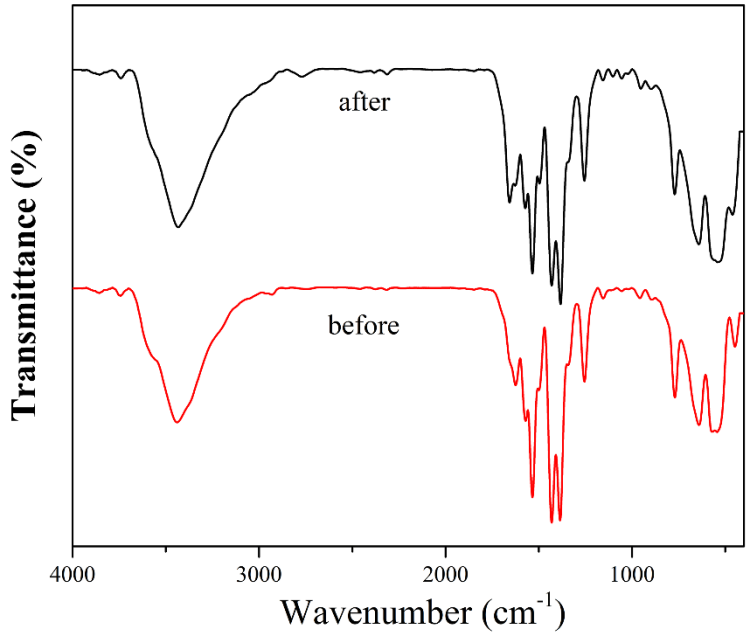

Figure S14. FT-IR spectra of NM_{111} before and after photocatalytic CO_2 reduction.

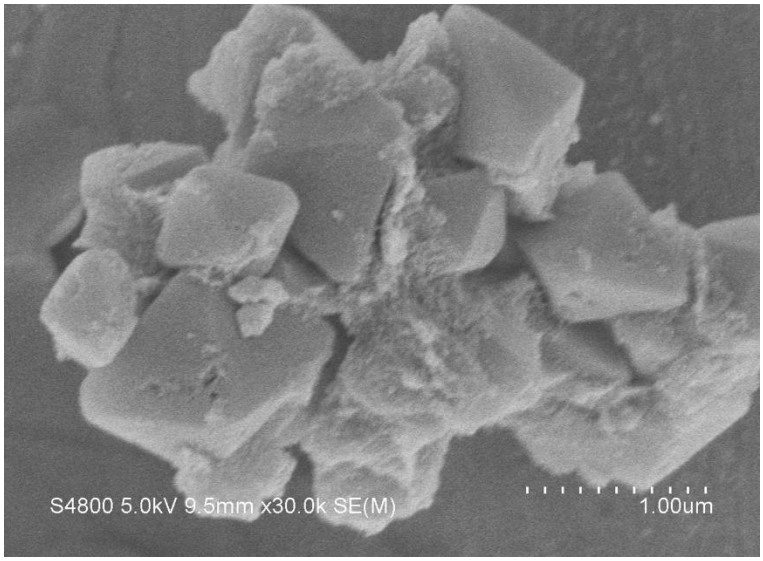

Figure S15. SEM of NM_{111} after photocatalytic CO_2 reduction.

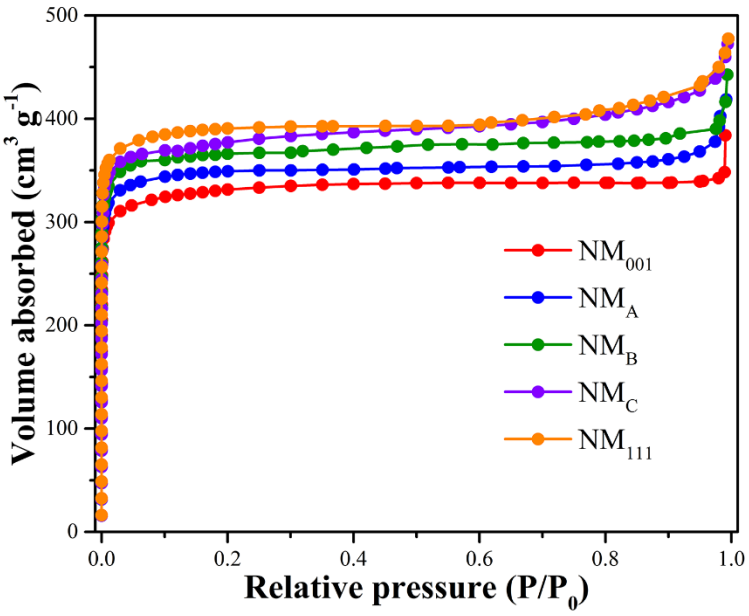

Figure S16. N_2 adsorption isotherms at 77 K of as-synthesized NH_2-MIL-125(Ti).

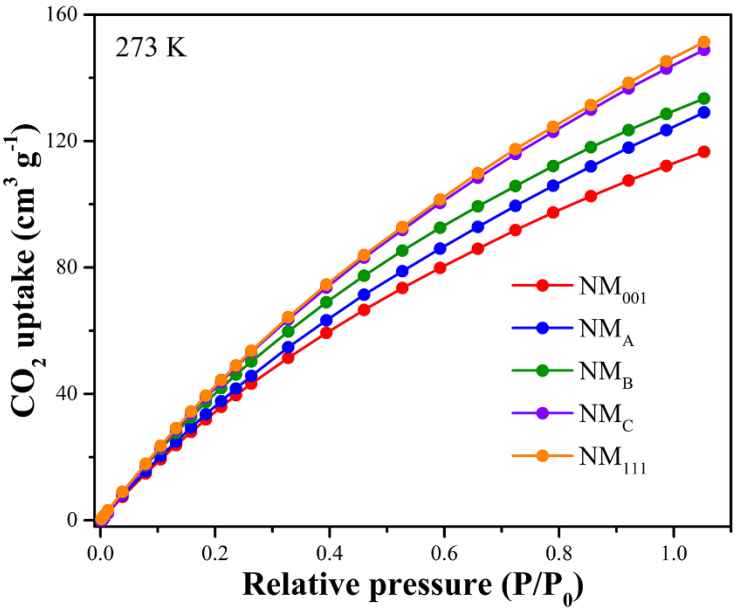

Figure S17. CO_2 adsorption isotherms at 273 K of as-synthesized NH_2-MIL-125(Ti).

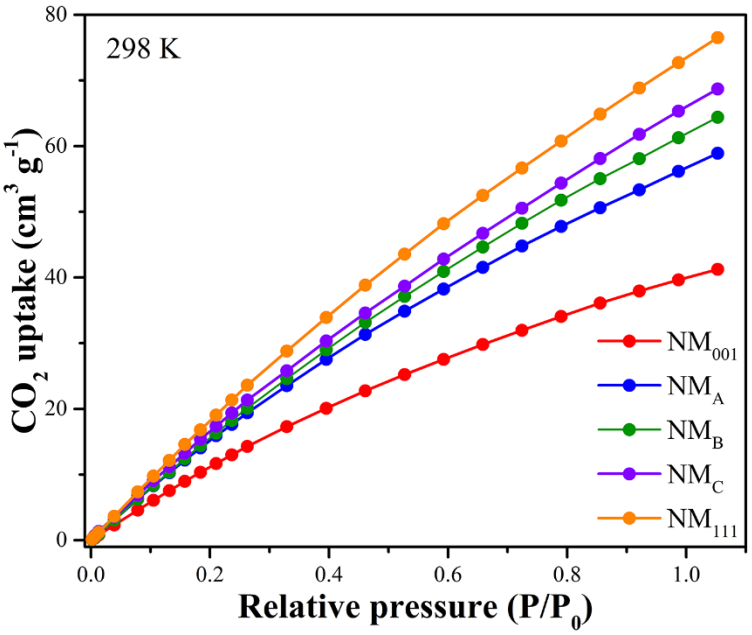

Figure S18. CO_2 adsorption isotherms at 298 K of as-synthesized NH_2-MIL-125(Ti).

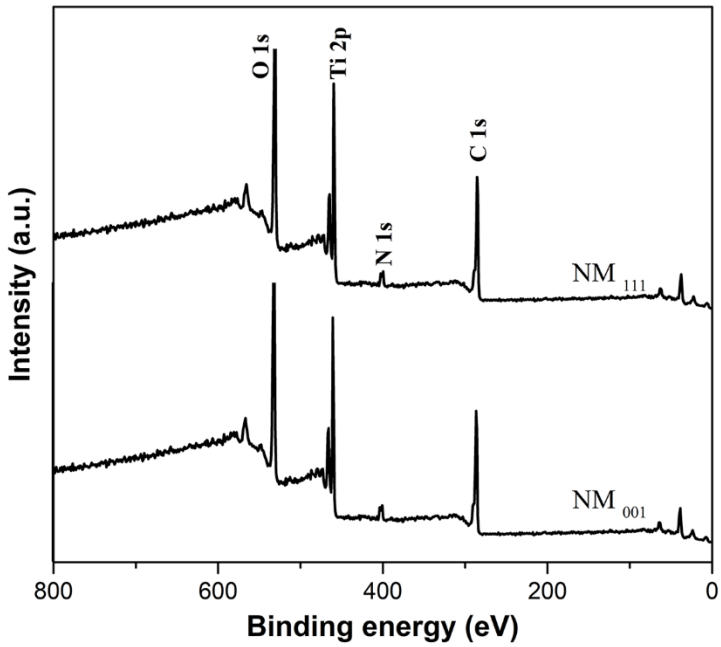

Figure S19. XPS survey spectra of as-synthesized NM_{001} and NM_{111}.

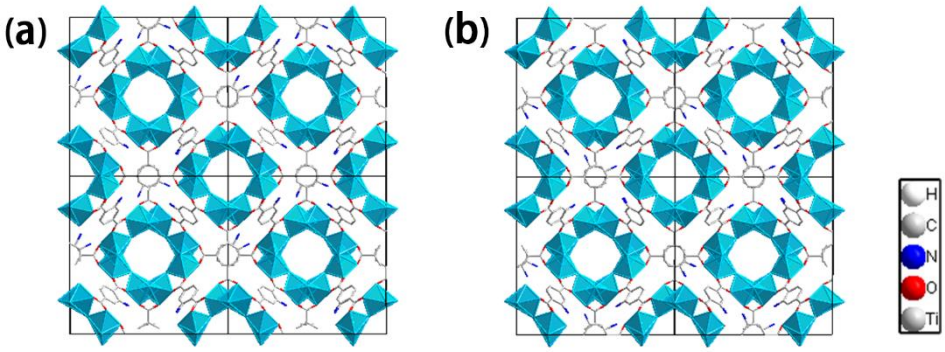

Figure S20. Structure of {001} facets in NH_2-MIL-125(Ti). (a) (001) (b) (00-1) crystallographic plane. For clarity, the hydrogen atoms are not shown.

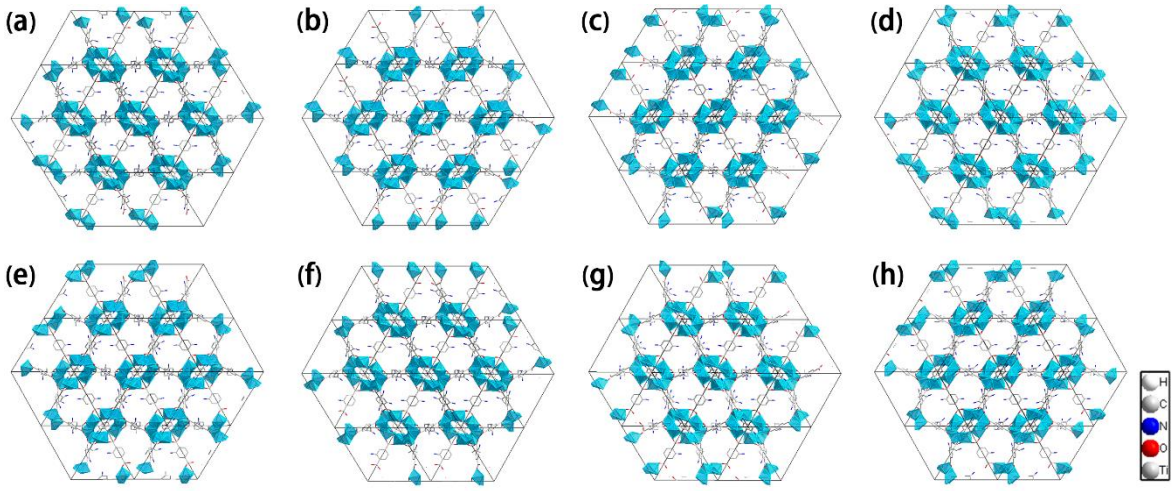

Figure S21. Structure of {111} facets in NH_2-MIL-125(Ti). (a) (111), (b) (1-1-1), (c) (11-1), (d) (1-11), (e) (-1-1-1) (f) (-111), (g) (-1-11) and (h) (-11-1) crystallographic plane. For clarity, the hydrogen atoms are not shown.

Table S1. The amounts of reactants and modulator in the photocatalysts synthetic system.

Samples	Titanium source (mM)	Acetic acid (AA) (mL)	NH_2-BDC (mM)	V_{DMF}/V_{MeOH} (V_{total}=10 mL)	Facets exposed
NM_{001}	TBOT (1.0)	0	3.0	7.0 / 3.0	{001}
NM_A	TPOT (1.0)	0	3.0	7.5 / 2.5	{001} {111}
NM_B	TPOT (1.0)	0	3.0	8.2 / 1.8	{001} {111}
NM_C	TPOT (1.0)	0	3.0	8.55 / 1.45	{001} {111}
NM_{111}	TPOT (1.0)	0.53	1.5	9.0 / 1.0	{111}

Table S2. Atomic concentration (%) of Ti, O, N and C in NM_{001} and NM_{111} determined by XPS analysis.

Samples	Ti (%)	O (%)	N (%)	C (%)
NM_{001}	6.84	26.78	7.09	59.29
NM_{111}	8.05	28.62	6.58	56.75

Table S3. Main characterization of as-synthesized photocatalysts used in this study.

Samples	{111} facets ratios %	S_{BET} (cm^2/g)	CO_2 uptake (cm^2/g)		Bandgap (eV)
			273 K	293 K	
NM_{001}	0	1124.16	116.50	41.24	2.62
NM_A	60	1190.18	129.06	58.91	2.69
NM_B	70	1264.42	133.46	64.40	2.65
NM_C	84	1290.07	149.68	68.70	2.66
NM_{111}	100	1312.19	151.33	76.51	2.75

Table S4. Quantum yield of CO and CH_4 production after 5 h reaction.

Samples	Φ_{CO} (%)	Φ_{CH4} (%)	Φ_T (%)
NM_{001}	0.016	0.012	0.028
NM_A	0.028	0.024	0.052
NM_B	0.040	0.032	0.072
NM_C	0.082	0.044	0.126
NM_{111}	0.140	0.068	0.208

Table S5. Summary of the total quantum yield for photocatalytic CO_2 reduction over various photocatalysts.

samples	Φ_T (%)	Reaction time	Light source	Ref.
NM_{001}	0.03	5 h	300 W Xe lamp (AM 1.5G)	This work
NM_A	0.05	5 h	300 W Xe lamp (AM 1.5G)	This work
NM_B	0.07	5 h	300 W Xe lamp (AM 1.5G)	This work
NM_C	0.13	5 h	300 W Xe lamp (AM 1.5G)	This work
NM_{111}	0.21	5 h	300 W Xe lamp (AM 1.5G)	This work
TiO_2	0.14	20 h	100 W high-pressure Hg lamp (UV irradiation)	10
Cu/TiO_2	0.27	20 h	100 W high-pressure Hg lamp (UV irradiation)	10
Ti-PS	0.17	6 h	300 W Xe lamp 250 nm <λ< 400 nm	11
Rh-Pd/ TiO_2	0.015	6 h	two 8 W UVA lamps (365 nm)	12

Table S6. Comparison of the photocatalytic CO_2 reduction by MOF-based photocatalysts.

samples	Photosensitizer	Products	$R_{electron}$ ($\mu mol\ g^{-1}h^{-1}$)	Ref.
NM_{111}	/	CO, CH_4	24.6	This work
$CsPbBr_3$/UiO-66(NH_2)	/	CO, CH_4	18.5	13
CuTCPP/UiO-66	/	CO	2.2	14
Co-UiO-67	$[Ru(bpy)_3]^{2+}$	CO	6585.0	15
Co-UiO-67	/	n.d.	/	
MOF-Cu	$[Ru(bpy)_3]^{2+}$	CO	68.0	16
MOF-Cu	/	n.d.	/	
CdS/Co-ZIF-9	bipyridine	CO	1120.0	17
Co-ZIF-9	bipyridine	n.d.	/	
CD@NH_2-UiO-66	CD	CO	33.2	18
NH_2-UiO-66	/	CO	7.0	

n.d.: not detectable.

The rate of electron consumption for photocatalytic reduced product, $R_{electron} = 2\times R(CO)+ 8\times R(CH_4)$, where R(CO) and $R(CH_4)$ are the formation rates ($\mu mol\ g^{-1}h^{-1}$) of the CO and CH_4, respectively.

Compared with other MOF-based photocatalysts, for example $CsPbBr_3$/UiO-66(NH_2), CuTCPP/UiO-66 and NH_2-UiO-66, strong catalytic ability of NM_{111} was found. For Co-UiO-67 and MOF-Cu catalysts, the photosensitizer was used in the photocatalytic reaction to increase the absorption of photons and trigger the reaction with high activity. For MOF-based

hybird photocatalysts, like CD@NH_2-UiO-66 and CdS/Co-ZIF-9, CdS and CDs (carbon dots) act as both electron receptors and photosensitizers. Meanwhile, CdS can be used as a photocatalyst in the reaction. Here, NM_{111}, a pure MOF photocatalyst can absorb light to stimulate the generation of electrons. The exposed {111} facets promote electron transfer and inhibit the recombination of electron-hole pairs, and show enhanced photocatalytic activity.

Reference

(1) Paulino, P.N.; Salim, V.M.M.; Resende, N.S.; Zn-Cu Promoted TiO_2 Photocatalyst for CO_2 Reduction with H_2O under UV Light. *Appl. Catal. B Environ.* **2016**, *185*, 362-370.

(2) Zhang, L.; Zhang, L.J.; Chen, Y.M.; Zheng, Y.K.; Guo, J.; Wan, S.L.; Wang, S.; Ngaw, C.K.; Lin, J.D.; Wang, Y. CdS/ZnO: A Multipronged Approach for Efficient Reduction of Carbon Dioxide under Visible Light Irradiation. *ACS Sustainable Chem. Eng.* **2020**, *8*, 5270-5277.

(3) Li, X.R.; Le, Z.Y.; Chen, X.L.; Li, Z.Q.; Wang, W.C.; Liu, X.Y.; Wu, A.; Xu, P.C.; Zhang, D.Q. Graphene Oxide Enhanced Amine-Functionalized Titanium Metal Organic Framework for Visible-Light-Driven Photocatalytic Oxidation of Gaseous Pollutants. *Appl. Catal. B Environ.* **2018**, *236*, 501-508.

(4) Martis, M.; Mori, K.; Fujiwara, K.; Ahn,W.-S.; Yamashita, H. Amine-Functionalized MIL-125 with Imbedded Palladium Nanoparticles as an Efficient Catalyst for Dehydrogenation of Formic Acid at Ambient Temperature. *J. Phys. Chem. C* **2013**, *117*, 22805-22810.

(5) Yang, Z.; Xu, X.; Liang, X.; Lei, C.; Cui, Y.; Wu, W.; Yang, Y.; Zhang, Z.; Lei, Z. Construction of Heterostructured MIL-125/Ag/g-C_3N_4 Nanocomposite as an Efficient Bifunctional Visible Light Photocatalyst for the Organic Oxidation and Reduction Reactions *Appl. Catal. B Environ.* **2017**, *205*, 42-54.

(6) Wang, X.; Maeda, K.; Thomas, A.; Takanabe, K.; Xin, G.; Carlsson, J.M.; Domen, K.;

Antonietti, M. A Metal-Free Polymeric Photocatalyst for Hydrogen Production from Water under Visible Light. *Nat. Mater.* **2009**, *8*, 76-80.

(7) Wang, S.; Yao, W.; Lin, J.; Ding, Z.; Wang, X. Cobalt Imidazolate Metal-Organic Frameworks Photosplit CO_2 under Mild Reaction Conditions. *Angew. Chem. Int. Ed.* **2014**, *53*, 1034-8.

(8) Zhang, H.; Wei, J.; Dong, J.; Liu, G.; Shi, L.; An, P.; Zhao, G.; Kong, J.; Wang, X.; Meng, X.; Zhang, J.; Ye, J.H. Efficient Visible-Light-Driven Carbon Dioxide Reduction by a Single-Atom Implanted Metal-Organic Framework. *Angew. Chem. Int. Ed.* **2016**, *55*, 14310-14314.

(9) Liu, Y.; Guo, J.H.; Dao, X.Y.; Zhang, X.D.; Zhao, Y.; Sun, W.Y. Coordination Polymers with a Pyridyl-Salen Ligand for Photocatalytic Carbon Dioxide Reduction. *Chem. Commun.* **2020**, *56*, 4110-4113.

(10) Li, Y.; Wang, W.-N.; Zhan, Z.; Woo, M.-H.; Wu, C.-Y.; Biswas, P. Photocatalytic Reduction of CO_2 with H_2O on Mesoporous Silica Supported Cu/TiO_2 Catalysts. *Appl. Catal. B Environ.* **2010**, *100*, 386-392.

(11) Ikeue, K.; Nozaki, S.; Ogawa, M.; Anpo, M. Charactrization of Self-Standing Ti-Containing Porous Silica Thin Films and Their Reactivity for the Photocatalytic Reduction of CO_2 with H_2O. *Catal. Today* **2002**, *74*, 241-248.

(12) Ola, O.; Maroto-Valer, M.; Liu, D.; Mackintosh, S.; Lee, C.-W.; Wu, J.C.S. Performance Comparison of CO_2 Conversion in Slurry and Monolith Photoreactors using Pd and Rh-TiO_2 Catalyst under Ultraviolet Irradiation. *Appl. Catal. B Environ.* **2012**, *126*, 172-179.

(13) Wan, S. P.; Ou, M.; Zhong, Q.; Wang, X. M. Peovskite-Type $CsPbBr_3$ Quantum Dots/UiO-66(NH_2) Nanojunction as Efficient Visible-Light Driven Photocatalyst for CO_2 Reduction. *Chem. Eng. J.* **2019**, *358*, 1287-1295.

(14) Wang, L.; Jin, P. X.; Duan, S. H.; She, H. D.; Huang, J. W.; Wang, Q. Z. In-Site Incorporation of Copper(Ⅱ) Porphyrin Functionalized Zirconium MOF and TiO_2 for Efficient

Photocatalytic CO_2 Reduction. *Sci. Bull.* **2019**, *64*, 926-933.

(15) Gao, X. S.; Guo, B.; Guo, C. M.; Meng, Q. D.; Liang, J.; Liu, J. X. Zirconium-Based Metal-Organic Framework for Efficient Photocatalytic Reduction of CO_2 to CO: the Influence of Doped Metal Ions. *ACS Appl. Mater. Interfaces* **2020**, *12*, 24059-24065.

(16) Wang, X. K.; Liu, J.; Zhang, L.; Dong, L. Z.; Li, S. L.; Kan, Y. H.; Li, D. S.; Lan, Y. Q. Monometallic Catalytic Models Hosted in Stable Metal-Organic Frameworks for Tunable CO_2 Photoreduction. *ACS Catal.* **2019**, *9*, 1726-1732.

(17) Wang, S. B.; Wang, X. C. Photocatalytic CO_2 Reduction by CdS Promoted with a Zeolitic Imidazolate Framework. *Appl. Catal. B Environ.* **2015**, *162*, 494-500.

(18) Li, S. M.; Ji, K.; Zhang, M.; He, C. S.; Wang, J.; Li, Z. Q. Boosting the Photocatalytic CO_2 Reduction of Metal-Organic Framework by Encapsulating Carbon Dots. *Nanoscale* **2020**, *12*, 9533-9540.